Water Permeation Drives Tumor Cell Migration in Confined Microenvironments

Kimberly M. Stroka,[1,2,3,7] Hongyuan Jiang,[4,6,7] Shih-Hsun Chen,[3] Ziqiu Tong,[1,2,3] Denis Wirtz,[1,2,3] Sean X. Sun,[1,2,4,5,*] and Konstantinos Konstantopoulos[1,2,3,5,*]

[1]Johns Hopkins Institute for NanoBioTechnology
[2]Johns Hopkins Physical Sciences-Oncology Center
[3]Department of Chemical and Biomolecular Engineering
[4]Department of Mechanical Engineering
[5]Department of Biomedical Engineering
The Johns Hopkins University, Baltimore, MD 21218, USA
[6]CAS Key Laboratory of Mechanical Behavior and Design of Materials, University of Science and Technology of China, Hefei, Anhui 230026, PRC
[7]Co-first author
*Correspondence: ssun@jhu.edu (S.X.S.), konstant@jhu.edu (K.K.)
http://dx.doi.org/10.1016/j.cell.2014.02.052

SUMMARY

Cell migration is a critical process for diverse (patho)physiological phenomena. Intriguingly, cell migration through physically confined spaces can persist even when typical hallmarks of 2D planar migration, such as actin polymerization and myosin II-mediated contractility, are inhibited. Here, we present an integrated experimental and theoretical approach ("Osmotic Engine Model") and demonstrate that directed water permeation is a major mechanism of cell migration in confined microenvironments. Using microfluidic and imaging techniques along with mathematical modeling, we show that tumor cells confined in a narrow channel establish a polarized distribution of Na^+/H^+ pumps and aquaporins in the cell membrane, which creates a net inflow of water and ions at the cell leading edge and a net outflow of water and ions at the trailing edge, leading to net cell displacement. Collectively, this study presents an alternate mechanism of cell migration in confinement that depends on cell-volume regulation via water permeation.

INTRODUCTION

Cell migration is a fundamental phenomenon that underlies diverse physiological and pathological processes such as tissue morphogenesis, immune response, and cancer metastasis. Much of what we know about the mechanisms of cell migration stems from in vitro studies with 2D substrates (Friedl and Alexander, 2011; Mogilner and Oster, 1996; Pollard and Borisy, 2003). The classical model of cell migration along 2D planar surfaces is characterized by cycles of actin polymerization-driven lamellipodial protrusion, integrin-dependent adhesion, myosin II-mediated contraction, and de-adhesion at the trailing edge.

Although 2D migration is relevant in certain processes, such as neutrophil migration along the endothelium or epithelial cell wound healing, most 2D assays fail to recapitulate the physiological tissue environment encountered in vivo (Wirtz et al., 2011).

Cells often migrate in vivo within 3D extracellular matrices (ECMs). Cells also migrate through 3D longitudinal tracks with bordering 2D interfaces (i.e., channels). These channels are formed between the connective tissue and the basement membrane of muscle, nerve, and epithelium (Friedl and Alexander, 2011). 3D longitudinal channels are also formed between adjacent bundled collagen fibers in fibrillar interstitial tissues. Importantly, cells have been reported to migrate through such 3D channels in vivo (Alexander et al., 2008). The cross-sectional areas (Wolf et al., 2009) of pores/channels encountered in vivo range from 10 to >300 μm^2, suggesting that cells migrating in vivo experience varying degrees of physical confinement. Mounting evidence suggests that physical confinement alters cell migration mechanisms (Balzer et al., 2012; Konstantopoulos et al., 2013; Pathak and Kumar, 2012; Stroka et al., 2013).

To isolate the effect of physical confinement that tumor cells experience as they migrate through the ECM microtracks in vivo, we have developed a chemotaxis-based microfluidic device containing microchannels of varying cross-sectional areas (Balzer et al., 2012; Tong et al., 2012). Migration of cells through wide microchannels (width by height = 50 × 10 μm^2) recapitulates the earmarks of 2D cell motility and depends on actin polymerization and myosin II-mediated contractility. However, metastatic breast cancer cells migrate through narrow (3 × 10 μm^2) microchannels even when actin polymerization, Rho/ROCK- or myosin II-dependent contractility, or β1-integrin function are inhibited (Balzer et al., 2012). Here, we present an actin- and myosin-independent mechanism of cell migration that is based on water permeation and active and passive ion transport in confined spaces.

Ion channels and aquaporins (AQPs) have previously been implicated in 2D cell migration (Papadopoulos et al., 2008; Schwab et al., 2007). However, their specific molecular roles during migration are not well understood. Cytoskeletal
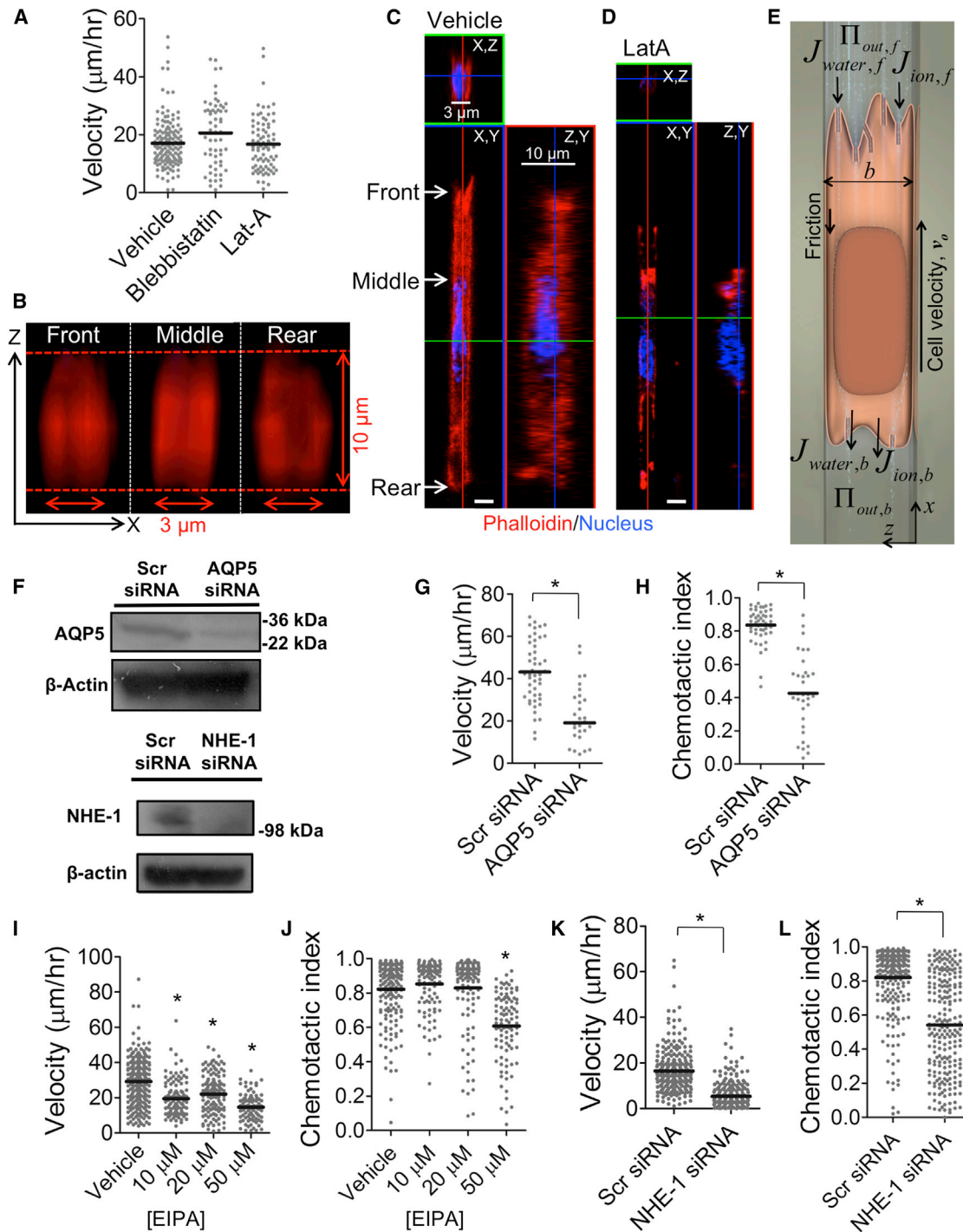
Figure 1. Migration in Confined Spaces Requires AQPs and Na⁺/H⁺ Exchangers but Not Actin Polymerization

(A) S180 cell velocity in the presence of 50 μM blebbistatin or 2 μM latrunculin-A (Lat-A). Each data point represents average velocity of one cell over the course of 2 hr. Horizontal bars indicate mean.

(B) Front, middle, and rear (X, Z) plane reconstructions of the actin cytoskeleton for the cell in (C).

(C) Vehicle control- or (D) Lat-A-treated S180 cells were stained for actin by phalloidin-Alexa 568, and cross-sections of confocal images are shown. White scale bars represent 3 μm.

(E) Schematic of the Osmotic Engine Model, based on water permeation through the cell membrane at leading and trailing edges.

(F) Immunoblots indicating knock down of AQP5 in MDA-MB-231 cells and NHE-1 in S180 cells.

(legend continued on next page)

components regulate the activity of ion channels (Dreval et al., 2005; Grunnet et al., 2002; Mazzochi et al., 2006), and as a result, volume regulation via these ion pumps requires an intact cytoskeleton. For example, the sodium hydrogen exchanger-1 (NHE-1) is known to physically interact with the actin cytoskeleton (Goss et al., 1994; Grinstein et al., 1993; Wakabayashi et al., 1992). Pharmacological inhibition of NHE-1 restrains leukocyte chemotaxis (Ritter et al., 1998) and the migration speeds of endothelial and epithelial cells (Klein et al., 2000). AQPs, transmembrane proteins that allow transport of water molecules across the cell membrane, are also involved in cell migration. Specifically, aquaporin 5 (AQP5) is overexpressed in lung and breast tumor cells and facilitates 2D migration of these cells (Chae et al., 2008; Jung et al., 2011), presumably by regulating water influx to facilitate protrusions by actin polymerization (Papadopoulos et al., 2008) and/or by stabilizing microtubules (Sidhaye et al., 2012). AQPs have been identified as potential targets for cancer therapeutic development, but like ion channels, their contribution to 2D versus confined migration is not well understood.

Here, we present an integrated experimental and theoretical approach showing that water permeation is a major mechanism of cell migration in confined microenvironments. We have termed this mode of migration the "Osmotic Engine Model," which is dependent on cell-volume regulation and the fluxes of ions and water into and out of the cell. Specifically, the polarized cell inside a narrow channel establishes a spatial gradient of ion channels and pumps in the cell membrane, creating a net inflow of water and ions at the cell leading edge and a net outflow of water and ions at the trailing edge. This leads to net cell displacement even when actin polymerization is inhibited. Because water flow is driven by osmotic pressure differences across the membrane (Lang et al., 1998), we hypothesized that external osmotic shocks at the leading and/or trailing edges of cells would have a strong influence on cell migration. Our Osmotic Engine Model predicts all key results pertinent to the application of osmotic shocks, which we have verified experimentally using a novel microfluidic device combined with cell engineering and microscopy techniques. Collectively, this study presents an alternate mechanism of migration in confined spaces that cells may exploit when actin polymerization is inhibited.

RESULTS

Role of Na$^+$/H$^+$ Exchangers and AQP5 in Migration through Confined Spaces

We have recently demonstrated (Balzer et al., 2012) and herein confirmed that confined migration of human metastatic MDA-MB-231 breast cancer cells persists even after actin polymerization or myosin II-mediated contractility is blocked (Figures S1A and S1B available online). We also validated these observations with mouse S180 sarcoma cells. We found no change in migration velocity for S180 cells treated with 50 μM blebbistatin or

2 μM latrunculin-A (Lat-A) relative to appropriate vehicle controls (Figure 1A), thereby confirming that neither myosin II-mediated contractility nor actin polymerization is required for migration in narrow channels. Actin filament disruption in Lat-A-treated S180 cells was confirmed via immunofluorescence microscopy by staining cells with Alexa-tagged phalloidin (Figures 1B–1D). Thus, we sought to develop an integrated theoretical and experimental approach to understand the mechanism by which tumor cells move through narrow channels even in the absence of actin polymerization and myosin II-mediated contractility.

Here we propose an Osmotic Engine Model that predicts that confined migration depends on the activity of transmembrane proteins responsible for water and ion flux through the cell membrane and does not directly require actin polymerization or actomyosin contractility. In this model, the polarized cell inside a confining channel establishes a spatial gradient of ion channels and pumps in the cell membrane, which results in a net inflow of water at the leading edge and a net outflow of water at the trailing edge (Figure 1E). We therefore examined the potential contributions of specific ion pumps and AQPs to confined cell migration. Although AQP1, AQP3, and AQP5 have been implicated in cancer, AQP5 expression is 3-fold higher than that of AQP1 and AQP3 in S180 (Figures S1E and S1F) and MDA-MB-231 cells (data not shown), thereby justifying our focus on AQP5. Knockdown of AQP5 in human MDA-MB-231 breast cancer cells, as confirmed via immunoblotting (Figure 1F), markedly suppressed cell migration velocity and chemotactic index in narrow channels (Figures 1G and 1H). We next chose to focus on Na$^+$/H$^+$ pumps, due to their established role in cell migration and volume regulation (Schwab, 2001; Schwab et al., 2012). Inhibition of Na$^+$/H$^+$ channels via the use of 5-(N-ethyl-N-isopropyl)amiloride (EIPA) reduced cell migration velocity and chemotactic index in a dose-dependent manner for both S180 (Figures 1I and 1J) and MDA-MB-231 cells (Figure S1C). The inhibitory effects of EIPA on cell migration were also observed in wide channels (Figure S1D). Of all Na$^+$/H$^+$ exchangers that are localized on the plasma membrane, NHE-1, -2, and -4 have been implicated in cancer (Beltran et al., 2008). Because the expression of NHE-1 on S180 cells is 5-fold higher than that of NHE-2 and -4 (Figures S1E and S1G), we examined its contribution to migration in confined spaces. Knockdown of NHE-1, as confirmed by immunoblotting (Figure 1F), reduced cell migration velocity and chemotactic index. This effect was comparable to that seen with the highest dose of the pharmacological inhibitor EIPA (50 μM) (Figures 1K and 1L), thereby suggesting the dominant role of NHE-1 among other Na$^+$/H$^+$ exchangers in migration through confined spaces. Collectively, these data reveal that NHE-1 and AQP5 regulate 2D and confined migration.

Theoretical Basis of the Osmotic Engine Model

The physics behind the Osmotic Engine Model is based on forces driving water flow across the membrane (Figure 2A)

(G and H) Velocity (G) and chemotactic index (H) of scramble control and AQP5-depleted MDA-MB-231 cells.

(I and J) Velocity (I) and chemotactic index (J) of S180 cells treated with increasing concentrations of EIPA.

(K and L) Velocity (K) and chemotactic index (L) of scramble control and NHE-1 siRNA-transfected S180 cells.

*p < 0.05 in comparison with control by Student's t test. All migration experiments were performed in 3 μm-wide channels. See also Figure S1.
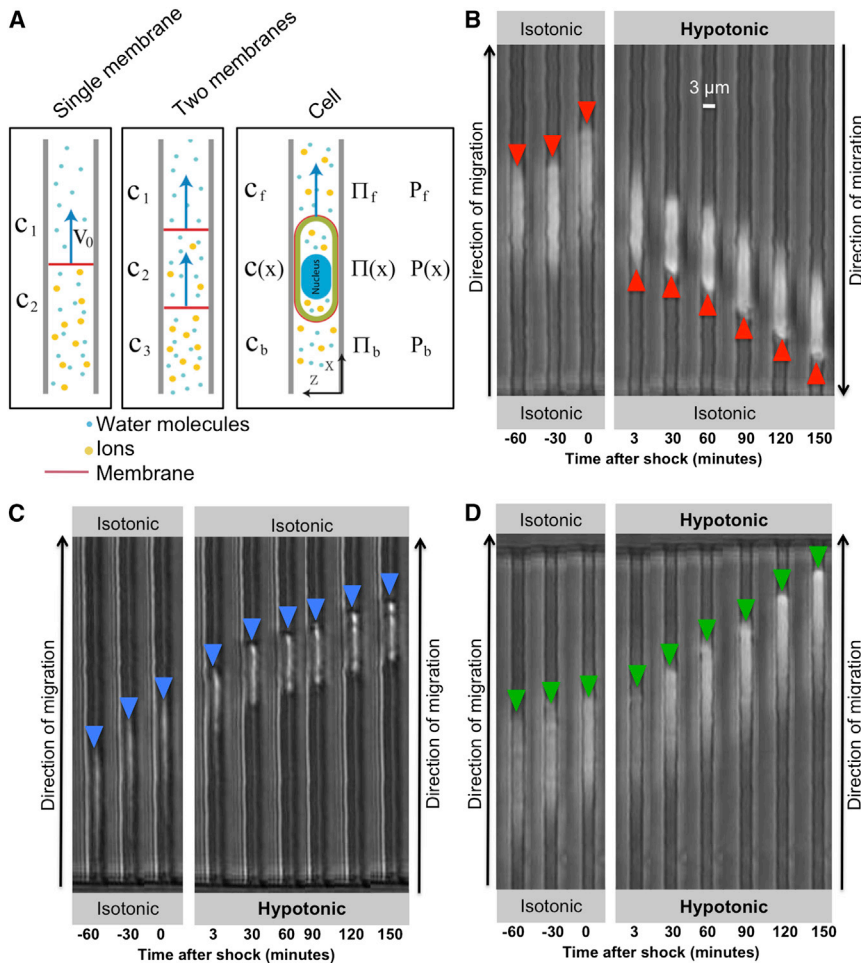
Figure 2. Localized Osmotic Shocks Influence Cell Migration in Confined Spaces

(A) Schematics showing the movement of a moveable semipermeable membrane, a vesicle enclosed by a semipermeable membrane, and a cell driven by osmotic pressure difference (see Extended Experimental Procedures for further explanation).

(B–D) Also shown are phase-contrast image sequences of S180 cells before shock and after (B) a hypotonic shock at the leading edge, (C) a hypotonic shock at the trailing edge, or (D) a hypotonic shock at both the leading and trailing edges. Hypotonic shock = 165 mOsm/l.

See also Figure S2 and Movie S1.

(Jiang and Sun, 2013). The water flow across a semipermeable membrane (permeable to water but not permeable to ions) is driven by the chemical potential difference across the surface, $\Delta\Psi = (\Delta P - \Delta\Pi)$, where ΔP is the hydrostatic pressure difference and $\Delta\Pi$ is the osmotic pressure difference. At equilibrium, the chemical potential is zero when the hydrostatic pressure difference exactly balances the osmotic pressure difference. Water is directly permeable to membranes, but AQP channels can further increase water permeability. In addition, eukaryotic cells have many different types of passive channels and active ion pumps that regulate the flow of ions and small solutes across the cell membrane (Figure 2A). Therefore, the cell can actively control the osmotic pressure difference, $\Delta\Pi$, as $\Delta\Pi = \Pi_{in} - \Pi_{out} = RT(c_{in} - c_{out})$, where c_{in} and c_{out} are ion concentrations inside and outside of the cell, respectively. By establishing polarized distributions of AQPs, passive ion channels, and active ion pumps, the cell can direct the water flow at the leading and trailing edges, which leads to overall translocation of the cell. Detailed descriptions of the physics are given in the Extended Experimental Procedures, and Table S1 contains a list of all parameters. Here we outline some essential features of the model.

To begin, we consider water fluxes at the front (leading edge) and back (trailing edge) (Figure 2A):

$$J_{water,f} = -\alpha_f \Delta\Psi_f \\ J_{water,b} = -\alpha_b \Delta\Psi_b, \qquad (1)$$

where (f,b) denotes the leading and trailing edges of the migrating cell, respectively, α_f and α_b are permeation constants related to the polarized distribution of AQPs at the front and back, and $\Delta\Psi_f$ and $\Delta\Psi_b$ are the water chemical potential differences across the membrane at the two edges. The water chemical potential is related to the hydrostatic $(\Delta P = P_{in} - P_{out})$ and osmotic pressure $(\Delta\Pi = \Pi_{in} - \Pi_{out})$ differences across the membrane. From the net volume change, we have:

$$\frac{dL}{dt} = (J_{water,f} + J_{water,b}), \qquad (2)$$

where L is the length (proportional to volume) of the cell. Importantly, by introducing FITC-dextran into the upper inlets of the device, we have experimentally verified that the cells completely occlude the channels (Figures S1H–S1J). The change in ion content is as follows:

$$\frac{dn}{dt} = S(J_{in,f} + J_{out,f} + J_{in,b} + J_{out,b}), \qquad (3)$$

where n is the number of solutes in the cell; n is related to c_{in} by $n = \int c_{in} \cdot S dx$. S is the channel cross-sectional area, and the ionic fluxes at the leading and trailing edges ($J_{in,f}$, $J_{out,f}$, $J_{in,b}$, and $J_{out,b}$) are given by Equations S4 and S5 in the Extended Experimental Procedures. If the cell is polarized, the flux parameters $(\alpha, \beta, \gamma, \Delta\Pi_c)$ introduced in the Extended Experimental Procedures would be different at the front and back, leading to different fluxes of ions and water at the leading and trailing edges. Net cell movement is achieved through control of the fluxes of ions and water at the leading and

trailing edges. Here, we assume that the flux parameters are constants; thus, we do not consider possible dynamics in polarization of the cell, though this may be explored in future work.

The movement of the cell is resisted by friction between the cell cortex and cell cytoplasm, plus the friction between the cell membrane and channel walls. Therefore, the tension, T, in the cell membrane and cortex balances these frictional forces:

$$\frac{\partial T}{\partial x} = \left(\frac{6\eta}{b} + \xi_w \right) v_0. \qquad (4)$$

Here, η is the viscous drag coefficient of the cytoplasm, ξ_w is the friction coefficient between the cell and the channel wall, and v_o is the velocity of the cell relative to the channel walls. If we regard the cortex as an elastic layer, then $T = \sigma h$, where σ is the cortical stress and h is the cortical thickness.

Because there are different ion and water fluxes at the leading and trailing edges, the hydrostatic pressure and ion concentration inside the cell are not uniform. These quantities can be modeled using the Stokes equation and the diffusion equation, respectively:

$$\nabla P = \eta \nabla^2 \mathbf{v}$$
$$\frac{\partial c}{\partial t} + \mathbf{v} \cdot \nabla c = D\nabla^2 c, \qquad (5)$$

where $\mathbf{v}$ is the cytoplasmic flow field, c is the cytoplasmic solute concentration, D is the diffusion constant, and P is the hydrostatic pressure of the cytoplasm. Given the flux boundary conditions, these equations can be solved if we assume that the concentration field equilibrates to steady state rapidly. The net average cytoplasmic velocity at steady state, $\bar{v} = 1/b \int_0^b v(z)dz$, should be zero. Therefore, solving the cytoplasmic velocity equation will determine the average velocity and the velocity of migrating cells. This set of equations closes the problem and provides a simple model of cell migration driven by fluid permeation. Thus, the cell migration speed is

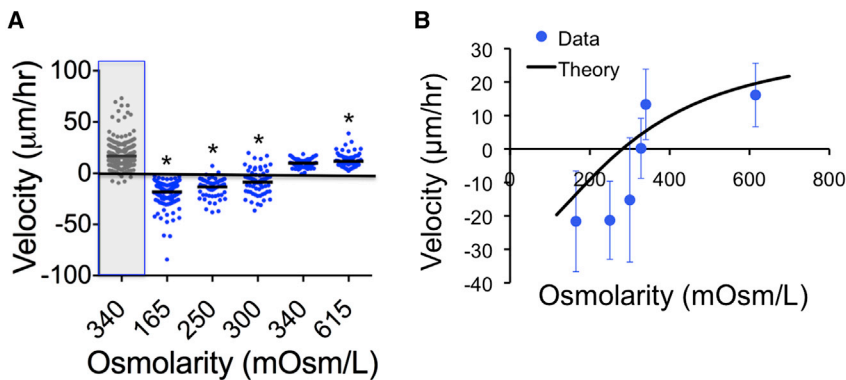## Osmotic Shocks Regulate Cell Migration Speed and Direction

If cells migrate in narrow channels using the osmotic engine mechanism, we would expect that the application of an osmotic shock influences cell motility even in the case where cell polarization remains unchanged. If the osmotic pressure outside the cell's leading edge ($\Pi_{out,f}$) decreases, or if the osmotic pressure outside the cell's trailing edge ($\Pi_{out,b}$) increases, the sign of the cell migration velocity could change, as suggested by Equation 6. Notice that $\Delta\Pi_c$ is proportional to Π_{out}, as explained in the Extended Experimental Procedures. Thus, the model predicts that application of a hypotonic shock at the leading edge or a hypertonic shock at the trailing edge of the cell may reverse the direction of cell migration. Although these results are not intuitive, they are testable with our microchannel device, which provides the ability to modulate the extracellular osmolarity distinctly at either the leading or trailing edge of the cells migrating through narrow channels (Figures S2A–S2C). To vary extracellular osmolarity, we added either deionized, filtered water or xylose to the culture medium to create hypotonic (85–328 mOsm/l) or hypertonic (375–615 mOsm/l) solutions, respectively (Figure S2D). Osmolarity was measured with an osmometer.

Using phase-contrast time-lapse microscopy, we tracked the migration of cells through narrow channels in an isotonic medium (340 mOsm/l) using FBS (10%) as a chemoattractant. As shown in Figure 2B and Movie S1, prior to the application of an osmotic shock, S180 cells migrated toward the chemoattractant (from bottom to top). At time $t = 0$, the medium at the top of the chamber (i.e., leading edge of the migrating cell) was changed to hypotonic (165 mOsm/l) and still contained 10% FBS, whereas an isotonic solution was maintained at the bottom of the chamber (Figure 2B). This osmotic shock caused a rapid reversal in cell migration direction (Figures 2B and 3A). The speed of migration in the opposite direction decreased progres-
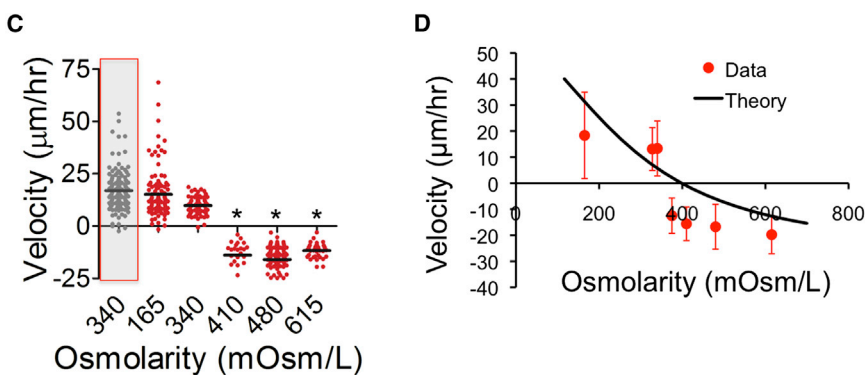
$$v_0 = \frac{b^2 h \alpha \left\{ 2D(\Pi_{out,b} - \Pi_{out,f}) + LRT[\gamma(\Delta\Pi_{c,f} - \Delta\Pi_{c,b}) + \beta(\sigma_{c,f} - \sigma_{c,b})] \right\}}{6bL^2 RT \alpha\beta\eta + 12hL\alpha\eta(2D + LRT\gamma) + b^2[4Dh + LRT(2h\gamma + L\alpha\beta\zeta_w)]}. \qquad (6)$$

The derivation and explanation of this analytical expression and the various terms are given in detail in the Extended Experimental Procedures, and parameters are listed in Table S1. Note that the cell velocity is only a function of the current cell length, L, which is proportional to cell volume. Also, the velocity is independent of the constitutive relation of the cell cortex or any active stress in the cortex. Therefore, the content of the cortex is unimportant, and the cortex simply balances the tension from frictional force. This model predicts that actin and myosin have no direct influence on the overall cell velocity. However, actin and myosin activity will influence the steady-

sively as the osmolarity of the medium approached isotonicity (Figure 3A). We confirmed that ~99% of cells remained viable throughout the full osmotic range, as assessed by the trypan blue exclusion assay (not shown). Most importantly, our experimental results agreed well with the theoretical predictions (Figure 3B).

The application of a hypotonic shock at the trailing edges of cells had no significant effect on migration direction (Figures 2C and 3C and Movie S1). Interestingly, a hypotonic shock at the cell trailing edge had similar effects as a hypertonic shock at the cell leading edge (Figures 3A–3D). Likewise, a hypertonic
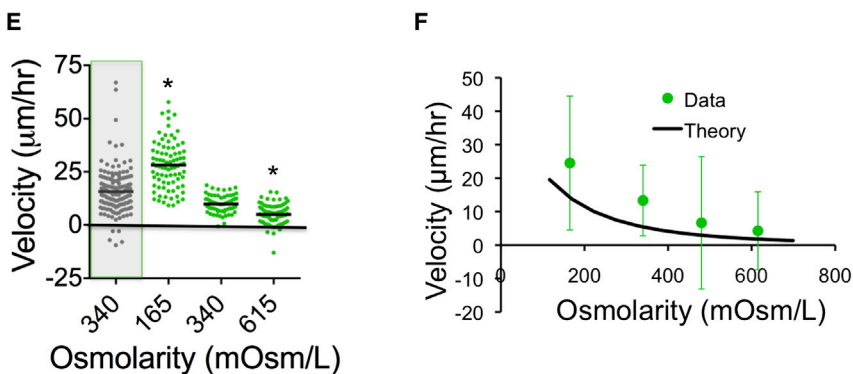
Leading edge

A

B

Trailing edge

C

D

Leading and trailing edge

E

F

Figure 3. The Osmotic Engine Model Predicts Cell-Velocity Patterns in Response to Osmotic Shocks

S180 cell velocity as a function of osmotic shock at the (A) leading edge, (C) trailing edge, or (E) both leading and trailing edges. In (A), (C), and (E), gray boxes indicate migration velocity before shock, whereas data with white background represent an osmotic shock (or media change only, in the case of 340 mOsm/l control). *p < 0.05 in comparison with control (340 mOsm/l postshock) by Student's t test. All migration experiments were performed in 3 μm-wide channels. Theoretical predictions using one set of parameters are also shown for velocity as a function of osmotic shock at the (B) leading edge, (D) trailing edge, or (F) both leading and trailing edges. Data points in (B), (D), and (F) represent mean ± SD. See also Figure S3.

that we used the same set of parameters (Table S1) for all fittings in this paper. Similar qualitative observations were made using MDA-MB-231 cells (Figures S3A–S3C) and human CH2879 chondrosarcoma cells (Figures S3D–S3F), though their sensitivities to osmotic shock vary between cell lines.

Cells Shrink in Response to Polarized Hypotonic Shock in Narrow Channels

Cell-volume regulation is dependent on water flux across the cell membrane, which is driven by osmotic pressure gradients (Lang et al., 1998). When a detached cell is abruptly suspended in a hypotonic medium, it typically responds by initially swelling due to water influx in order to equilibrate intracellular and extracellular osmotic pressure, followed by regulatory volume decrease through release of ions, which brings the cell nearly back to its original volume (Stewart et al., 2011; Wehner et al., 2003). Indeed, we confirmed these results and observed an osmolarity-dependent increase in average cell volume several minutes

shock at the trailing edge reversed migration direction (Figures 3C and 3D) as did a hypotonic shock at the leading edge (Figures 3A and 3B). Finally, when cells were shocked at both the leading and trailing edges with either hypotonic or hypertonic media, there was no change in direction of migration (Figures 2D, 3E, and 3F and Movie S1). In all cases, the average speed of migration during the first 30 min after osmotic shock was a function of the osmolarity, and all sets of data agree well with the quantitative predictions of the model (Figures 3B, 3D, and 3F). It should be noted

after placing the cells into a hypotonic medium (Figures S4A and S4B).

Interestingly, our model predicts a counterintuitive overall *decrease* in cell length (and volume) following a hypotonic shock at either end of the cell within a confining microchannel. We thus experimentally quantified cell length as a function of time before and after osmotic shock. Because S180 cells completely occupied the cross-sectional area of the narrow microchannels as indicated by the lack of FITC-dextran flow around the cell (Figures S1H–S1J), cell length multiplied by the width and height
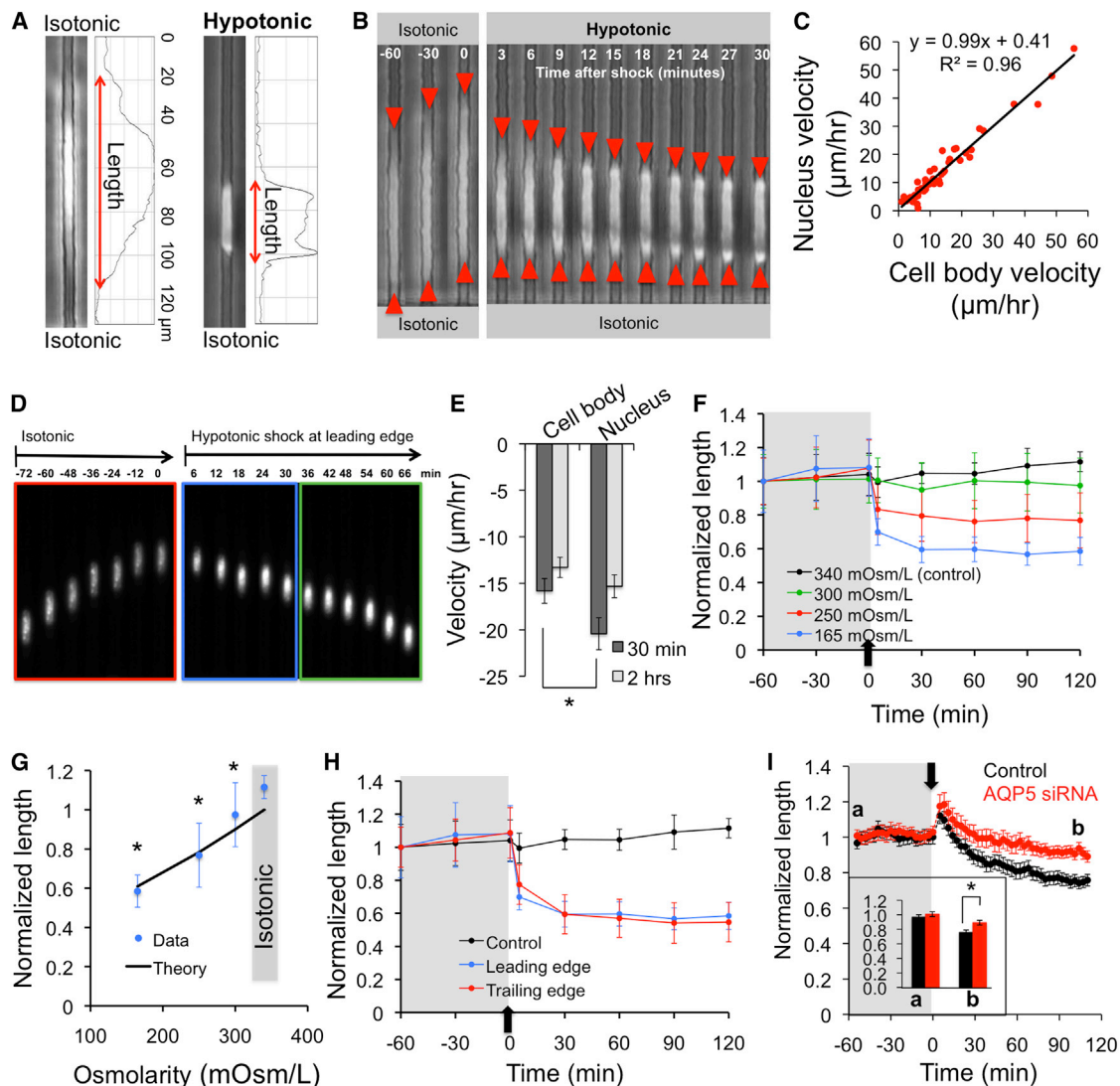
Figure 4. Hypotonic Shocks Produce a Nonintuitive Decrease in Cell Volume during Migration in Confined Spaces

(A) S180 cell length was computed based on the plot profiles of phase-contrast images.

(B) Phase-contrast sequence indicating the decrease in S180 cell length, mostly from the original leading edge, following a hypotonic shock (165 mOsm/l) at the leading edge.

(C) Nucleus versus cell-body velocity for S180 cells before osmotic shock.

(D and E) Fluorescence images of nucleus translocation in S180 cells (D) and velocities (computed over first 30 min or 2 hr) of cell body and nucleus (E) after a hypotonic shock at the leading edge. Bars indicate mean ± SEM, *p < 0.05.

(F) S180 cell length normalized to initial value (at $t = -60$ min, preshock) as a function of time before and after various hypotonic shocks at the leading edge.
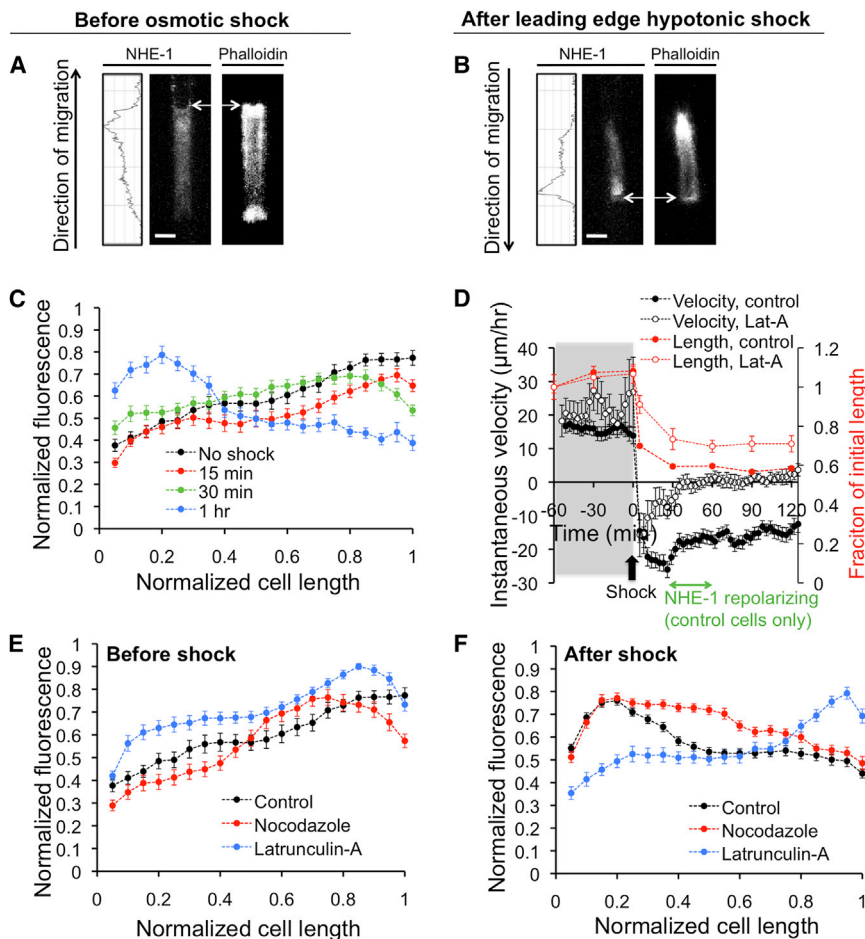
(G) Normalized lengths of S180 cells at equilibrium ($t = 120$ min) following a hypotonic shock at the leading edge, overlaid with the theoretical prediction.

(H) Normalized S180 cell length as a function of time before and after a hypotonic (165 mOsm/l) shock at the leading or trailing edge.

(I) Normalized control and AQP5-depleted MDA-MB-231 cell length as a function of time before and after a hypotonic (165 mOsm/l) shock at the leading edge. Data points represent mean ± SD. *p < 0.05 in comparison with (G) isotonic case or (I) scramble control by Student's t test. All migration experiments were performed in 3 μm-wide channels. See also Figure S4.

of the microchannels provides an estimate of cell volume (with an estimated error of 10% accounting for cell protrusions) inside the channel. We then combined phase-contrast imaging with quantitative image analysis to measure the length (and thus the volume) of cells live during migration within the confining channels before and after an osmotic shock (Figure 4A). Notably, after a

hypotonic shock at the leading edge, we observed a significant osmolarity-dependent decrease in cell length that did not recover, even 2 hr after the onset of shock (Figures 4B and 4F). Cell body and nucleus velocity were highly correlated during migration in isotonic media (Figure 4C); however, the nucleus traveled faster than the cell body during the first 30 min after a

Figure 5. NHE-1 Polarizes to the Leading Edges of Cells Migrating in Confinement

(A and B) Confocal images and corresponding NHE-1 plot profiles of S180 cells stained for NHE-1 or for actin by phalloidin-Alexa 488, (A) in isotonic medium or (B) after a hypotonic shock at the leading edge. White scale bars represent 3 μm, whereas white arrows point to cell's leading edge.

(C) Normalized NHE-1 fluorescence intensity (to maximum value for each cell) as a function of the normalized cell length (to maximum cell length), for isotonic conditions, or at various time points following a hypotonic shock at the leading edges of S180 cells.

(D) Instantaneous velocity (primary y axis) and normalized cell length (secondary y axis) as a function of time before and after a hypotonic shock at the leading edge of control and Lat-A-treated S180 cells. Data points represent mean ± SEM of at least 150 cells. The time during which NHE-1 repolarizes in control cells, according to (C), is indicated in green in this panel.

(E and F) Also shown are plots of normalized fluorescence intensity as a function of normalized cell length for control-, nocodazole-, or Lat-A-treated S180 cells (E) in isotonic conditions or (F) after a hypotonic shock at the leading edge.

In (C), (E), and (F), data points represent mean ± SEM of at least 30 cells. All experiments were performed in 3 μm-wide channels. Hypotonic shock = 165 mOsm/l. See also Figure S5.

hypotonic shock at the leading edge, whereas no difference was noted after 2 hr (Figures 4D and 4E). During the first 30 min, the displacement of the cell centroid was primarily due to cell shrinkage at the preshock leading edge and was accompanied by little to no displacement of the "new" leading edge (Figure 4B). This resulted in repositioning of the nucleus and faster nucleus velocity at 30 min postshock (Figures 4D and 4E). The nucleus velocity matched that of the cell body at later time points (Figure 4E) when the cell length reached an equilibrium (Figure 4F), as discussed below (Figure 5D). Decreases in cell length were also measured for cells migrating within an even more physically restrictive microchannel (width by height = 3 × 6 μm²) (Figure S4C); these results confirmed that observed decreases in cell length following osmotic shock were not simply due to cell rounding (i.e., increases in cross-sectional area) within the channels but were due to actual changes in cell volume. In accord with theoretical predictions, the equilibrium cell length decreased with decreasing osmolarity at the leading edge (Figure 4G). A similar decrease in cell length was also observed for cells hypotonically shocked at the trailing edge (Figure 4H). Collectively, our results indicate that application of a hypotonic shock at either the leading or trailing edge causes cell shrinkage. An explanation for this phenomenon is described in the

Extended Experimental Procedures. We verified these observations with MDA-MB-231 cells (Figure 4I). Most importantly, AQP5 depletion significantly suppressed the cell volume decrease induced by a hypotonic shock in MDA-MB-231 cells (Figure 4I).

Cell Volume Is Inversely Correlated with Migration Speed before and after Osmotic Shock

The model predicts that cell migration velocity weakly depends on cell volume inside the microchannel (Figure S4). In general, there existed a wide distribution of volumes within a suspended cell population (Figure S4B), which led to a wide distribution of lengths within the population of cells confined in the microchannels (Figures S4D–S4F). Consistent with theoretical predictions, we observed a weak but significant negative correlation (p < 0.05) between the magnitude of S180 cell speed and volume during preshock migration (Figure S4D), as well as after a hypotonic shock at either the leading edge (Figure S4E) or trailing edge (Figure S4F). We also observed a wide distribution in cell speeds (Figures S4D–S4F), in accord with the heterogeneity of cell size. Thus, smaller cells migrated faster within the microchannels.

NHE-1 and AQP5 Polarize to the Leading Edges of Cells Migrating in Narrow Channels

According to the model, the cell migration velocity is zero if the flux parameters $(\alpha, \beta, \gamma, \Delta \Pi_c)$ are uniform throughout the cell.

A nonzero velocity can be achieved if these parameters are different at the leading and trailing edges, presumably because of cell polarization. We thus determined whether cells migrating in confinement displayed a polarization of ion pumps and AQPs. We focused on NHE-1 due to its dominant role in S180 migration through confined spaces (Figures 1K and 1L). Confocal microscopy of NHE-1-immunostained S180 cells revealed a polarized distribution of NHE-1 at the cell leading edge during migration in an isotonic medium (Figures 5A and 5C). Importantly, application of a hypotonic shock at the top of the chamber induced reversal of cell migration direction (Figure 2B) and repolarization of NHE-1 to the new leading edge (same as preshock trailing edge) (Figures 5B and 5C). NHE-1 repolarization did not occur immediately but rather required 30–60 min after the application of the osmotic shock (Figure 5C). Similar observations for the NHE-1 spatial distribution before and after an osmotic shock were made for MDA-MB-231 cells (Figures S5A–S5C). It is noteworthy that not only NHE-1 but also AQP5 polarized to the leading edges of MDA-MB-231 cells preshock and repolarized to the new leading edges after a hypotonic shock at the top of the chamber (Figures S5D–S5F). NHE-1 in cells on a 2D planar surface was more uniformly distributed, with intense staining at both cell ends (Figures S5G and S5H).

It is worth noting that the Osmotic Engine Model applies to the time regime prior to ion channel or AQP repolarization, as the permeation constants (α, β, γ) do not change as a function of osmotic shock in the model. Because NHE-1 did not repolarize during the first 30 min after a 165 mOsm/l shock at the leading edge (Figure 5C), we considered the average experimental cell velocity during only the first 30 min postshock (Figures 3B, 3D, and 3F) rather than the overall cell velocity for the entire 2 hr duration that included repolarization of NHE-1 (Figures 3A, 3C, and 3E). Interestingly, cells experienced a migration surge in the opposite direction during the first 30 min postshock, according to a plot of instantaneous velocity versus time (Figure 5D). This surge correlated with the time course of the cells' volume decrease postshock (Figures 4B and 5D). These changes in velocity and cell volume are at the heart of the Osmotic Engine Model, where the cell quickly expels water from the original leading edge, propelling the cell in the opposite direction.

NHE-1, AQP5, and Actin Polymerization Are Involved in Cell Migration Response to Hypotonic Shock at Leading Edge

We next investigated the role of the cytoskeleton in establishing NHE-1 polarity in S180 cells. Before osmotic shock, NHE-1 polarized to the leading edges of cells migrating in confined channels even in the presence of nocodazole or Lat-A (Figure 5E), suggesting that the NHE-1 gradient is established during the initial stages of cell entry into narrow channels. Interestingly, after application of a hypotonic shock at the top chamber, Lat-A, but not nocodazole, treatment inhibited the repolarization of NHE-1 to the new leading edge (Figure 5F), indicating that actin polymerization plays a key role in repolarization.

Because NHE-1 and AQP5 are involved in confined cell migration (Figures 1 and S1), we next evaluated whether disruption of these proteins affected cell migration velocity after a hypotonic shock at the leading edge. Using a trypan blue assay, we first

verified that cell viability remained above 95% for the drug concentrations (e.g., Lat-A and EIPA) and osmolarities used in our experiments (data not shown). Following a hypotonic shock at the leading edge, S180 cell migration speed (in the opposite direction) and chemotactic index in 3 μm channels decreased with increasing EIPA doses (Figures 6A and 6E) or after knockdown of NHE-1 (Figures 6B and 6F). Furthermore, combinatorial treatment with 20 μM EIPA and 2 μM Lat-A nearly completely abrogated cell migration postshock (Figure 6A). Treatment with 10 μM EIPA or knockdown of AQP5 reduced the fraction of MDA-MB-231 cells that reversed direction after a 165 mOsm/l shock at the leading edge (Figures S6A and S6B).

Though Lat-A did not affect S180 cell migration velocity before osmotic shock, we did observe a reduction in the speed (Figure 6C) and chemotactic index (Figure 6G) of cells in the opposite direction after a hypotonic shock at the leading edge. In particular, Lat-A-treated cells still experienced the first "fast" phase of migration postshock, but the speed quickly decreased to a steady-state value close to zero within 30 min postshock (Figure 5D). Thus, although actin is not required in directionally persistent confined migration, it is critically involved during a response to osmotic shock in confined microenvironments, which also agrees with the fact that NHE-1 did not repolarize in Lat-A-treated S180 cells after a hypotonic shock at the leading edge (Figure 5F). Meanwhile, blebbistatin had no effect on cell velocity or chemotactic index postshock (Figures 6C and 6G). Nocodazole reduced cell migration speed postshock (Figure 6D) without affecting the chemotactic index (Figure 6H), though the decrease in migration speed was less drastic in comparison with before shock (Figures S6C and S6D). To rule out the possibility of cell migration being driven by a pressure gradient within the microfluidic device, we demonstrated that cell migration persists even in the absence of fluid flow from inlets to outlets (Figure S6E), and that a lack of the FBS chemoattractant drastically reduces cell migration velocity (Figure S6E) and chemotactic index (Figure S6F).

DISCUSSION

We recently demonstrated that actin polymerization and myosin II-mediated contractility may not be required for some cells in confined migration (Balzer et al., 2012). Here, we present an alternative mechanism for migration through confined spaces that is based on a net inflow of water at the cell leading edge and a net outflow of water at the trailing edge. A rigorous theoretical framework of the Osmotic Engine Model is consistent with all experimental data pertinent to the application of osmotic shocks in cells migrating inside physically constricted spaces. Our major observations aligning the theory and experiments are the following: (1) volume-regulating ion pumps and AQPs are involved in migration through confined spaces; (2) ion pumps and AQPs polarize to the leading edges of confined cells; (3) cells reverse direction when hypotonically shocked at the leading edges or hypertonically shocked at the trailing edges; (4) migration direction does not change when cells are hypotonically shocked at the trailing edges or hypertonically shocked at the leading edges; (5) cell volume decreases upon hypotonic shock in confinement; and (6) cell migration speed is weakly correlated
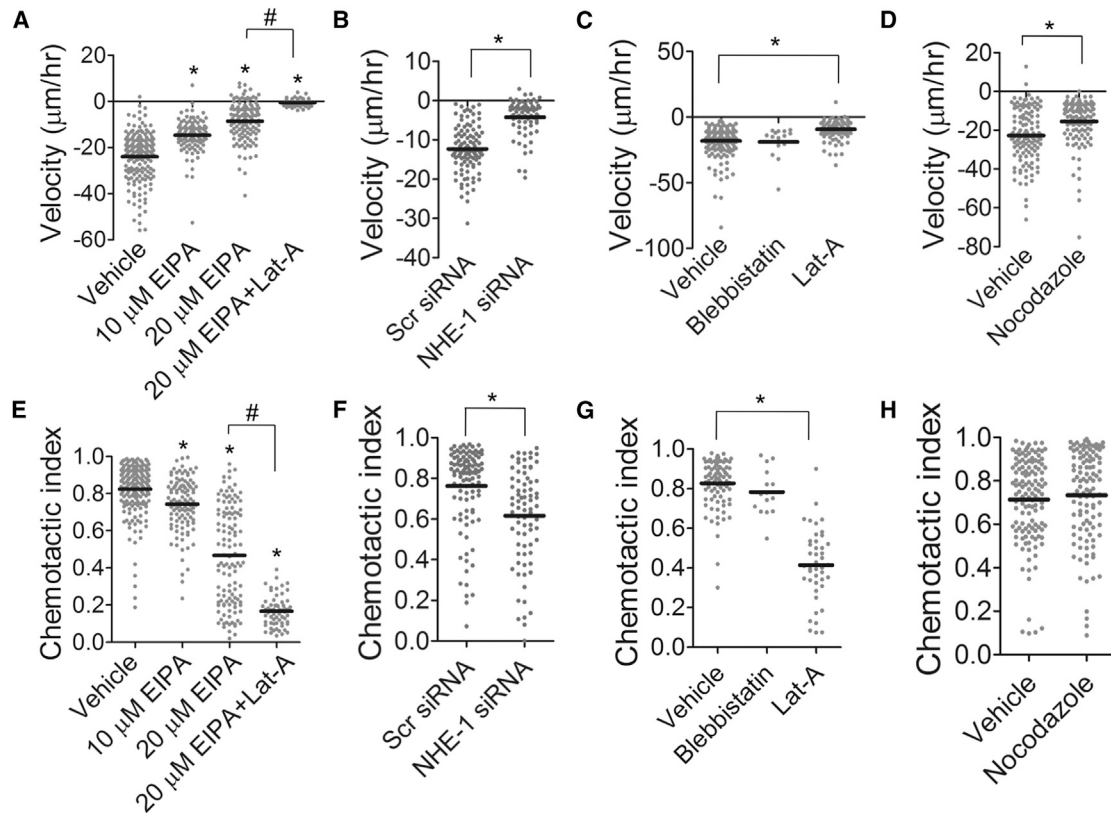
Figure 6. Cell Migration in Confinement after an Osmotic Shock Depends on an Interplay between Na⁺/H⁺ Exchangers and Actin Polymerization

(A–D) Velocity for (A) EIPA- or EIPA+Lat-A-, (B) NHE-1 siRNA-, (C) blebbistatin- or Lat-A-, and (D) nocodazole-treated S180 cells migrating in 3 μm channels.

(E–H) Also shown is the chemotactic index for (E) EIPA- or EIPA+Lat-A-, (F) NHE-1 siRNA-, (G) blebbistatin- or Lat-A, and (H) nocodazole-treated S180 cells.

*$p < 0.05$ in comparison with control by ANOVA followed by Tukey test (A and E) or Student's t test (B, C, D, F, G, and H). #$p < 0.05$ between groups indicated. All migration experiments were performed in 3 μm-wide channels. See also Figure S6.

with cell volume. Our model qualitatively predicts many nonintuitive results by capturing the key physics behind cell migration in confined spaces. This is an illustration of why theory is needed to explain complex biological phenomena. Our current model does not account for all possible ions, channels, and AQPs; a full model will require charged ions and consideration of voltages across the cell membrane.

The Osmotic Engine Model predicts that a nonzero cell velocity can be achieved in confined spaces as a result of (1) different extracellular osmolarities at the cell's leading and/or trailing edges and/or (2) spatial polarization of ion channels and AQPs along the longitudinal cell axis. During chemoattractant-driven migration in isotonic media, NHE-1 and AQP5 are polarized at the leading edge (i.e., both γ and α have distinct values at the front and rear of the cell), resulting in a positive velocity. During the first 30 min after a hypotonic shock at the leading edge, the extracellular osmolarity at the postshock leading edge is higher than that of the trailing edge (i.e., Π_{out} and $\Delta\Pi_c$ are different at the front and rear of the cell). This difference enables cell migration in the opposite direction away from the chemoattractant, and it can occur even though NHE-1 and AQP5 have not yet repolarized during the first 30 min

postshock. In other words, because $\Delta\Pi_c$ is proportional to Π_{out}, the model correctly predicts that a hypotonic shock at the leading edge results in a reversal of cell direction. These theoretical and experimental observations illustrate that the differences in osmolarity at the leading and trailing edges of the cell can "override" the lack of spatial polarization of the ion pumps and AQPs to the leading edge. At later time points (t > 30 min postshock), redistribution of NHE-1 and AQP5 at the new leading edge occurs. The slight decrease in cell-body velocity noted at t > 30 min postshock may be attributed to the presence of the adverse chemoattractant gradient. Ion-pump and AQP polarization are key for migration in confined spaces possibly due to the geometrical constraints of cells squeezed into a longitudinal channel, where the cell width is much shorter than the length compared to the 2D case (Hung et al., 2013). As a result, water influx and efflux are directed along a single axis along the length of the confined cell, allowing water permeation to be a major mechanism driving cell migration within the microchannel. A similar mechanism is not possible on 2D planar surfaces without actin polymerization to guide the protrusions. In vivo, cells likely employ a combination of migration mechanisms, with water permeation being one of them,

especially in 3D longitudinal tracks created by anatomical structures.

The decrease in volume observed after application of a hypotonic shock at the leading edge in microchannels is presumably due to water expulsion at the preshock leading edge, which drives the cell in the opposite direction. Indeed, AQP5 depletion suppresses both the fraction of cells reversing direction as well as the decrease in cell volume induced by the application of a hypotonic shock. The reversal of cell migration does not require actin within the first 30 min after osmotic shock, as predicted by the model, though our Lat-A experiments show that actin polymerization is necessary to establish the repolarization of NHE-1 following an osmotic shock. Note that Lat-A may also perturb ion-channel function.

Polarization of ion channels is typically associated with axonal trafficking in neurons (Chung et al., 2006). However, the role of ion channels and AQPs in cell migration has been largely underappreciated, even on 2D planar surfaces, where water permeation facilitates actin polymerization and volume regulation (Papadopoulos et al., 2008). Furthermore, a mechanism that directly requires ion-channel and AQP polarization and activity without the need for actin polymerization has never been put forth. Previous theoretical models have considered water transport only while neglecting active and passive transport of ions as well as the mechanics of the cell cortex (Jaeger et al., 1999) or have considered cytoskeletal dynamics without accounting for water or ion-channel activity (Taber et al., 2011). Theoretical models have also shown that fluid flow can be driven by two chemically reacting molecular species and osmotic effects (Atzberger et al., 2009), and that a body immersed in a very viscous fluid can swim by drawing in and expelling fluid at different locations along its cell surface (Spagnolie and Lauga, 2010); however, these models have not identified the mechanism governing the fluid flow. Recent experimental work has suggested that neutrophil-like cells migrating in confined spaces push water ahead, generating a hydraulic pressure (Prentice-Mott et al., 2013). It has also been proposed that actin polymerization upsets the local cellular osmotic pressure equilibrium, and the resulting unbalanced osmotic force drives cell protrusion (Oster and Perelson, 1987). In addition, recent studies have shown that significant pressure gradients and fluid flow can occur in cells, presumably through myosin-dependent contraction (Charras et al., 2005; Iwasaki and Wang, 2008; Keren et al., 2009; Mitchison et al., 2008). In particular, NHE-1 activity has been proposed to influence cell swelling and hydrostatic pressure gradients in order to facilitate local protrusions (Mitchison et al., 2008). Importantly and uniquely, our model based on water and ion-channel polarization can explain the actin- and myosin II-independent migration that occurs in narrow channels.

Although our model qualitatively predicts all trends in S180 and CH2879 cell migration pertinent to osmotic shocks, it does not completely predict migration behavior of MDA-MB-231 cells. Although MDA-MB-231 cells can still migrate in the absence of actin polymerization, the decrease in migration speed suggests that there may be an actin-driven component. Meanwhile, inhibition of actin polymerization in S180 or CH2879 cells does not affect migration speed during normal migration. Thus, our model

is most applicable to and correctly predicts behavior in S180 cells, which migrate independently of actin polymerization; however, water permeation also plays a critical role in migration and volume regulation of MDA-MB-231 cells.

Ion channels may become polarized to the leading edge by vesicular transport along microtubules, in accompaniment with actin polymerization, through diffusion, or by some other unknown mechanism. For example, microtubule transport facilitates delivery of post-Golgi carriers (Yadav et al., 2009), recycling endosomes (Palamidessi et al., 2008), and mRNA (Mingle et al., 2005) to the cell's protruding edge. The fact that inhibition of microtubule polymerization by nocodazole reduced migration speed before and after osmotic shock indicates that microtubules are indeed involved in confined cell migration. However, nocodazole did not interfere with NHE-1 polarization before shock or repolarization after osmotic shock, suggesting that microtubules are not responsible for setting up NHE-1 gradients within cells. Rather, actin polymerization is likely accountable, as Lat-A prevented repolarization of NHE-1 upon osmotic shock at the leading edge. Therefore, our data suggest that actin polymerization helps the cell to establish initial ion-channel and AQP polarization, but once that is completed, the major mechanism for migration is water permeation rather than actin polymerization. The specific mechanism by which actin polymerization drives NHE-1 repolarization could be the focus of future work.

In conclusion, we have put forth an alternative mechanism in which a confined cell establishes a spatial gradient of ion channels and pumps in the cell membrane, creating a net inflow of water at the cell leading edge and a net outflow of water at the trailing edge, which leads to net cell displacement even when actin polymerization is inhibited. We demonstrated theoretically and experimentally that a nonzero velocity can be achieved in confined cells as a result of either (1) different extracellular osmolarities at the cell's leading and trailing edges or (2) different numbers of ion channels and AQPs at the cell's leading and trailing edges. This model may be relevant during in vivo situations where cells migrate through existing tracks in the extracellular space. Due to the pronounced role of Na^+/H^+ ion channels and AQPs in tumor cell migration, our model may be exploited for future development of cancer therapeutics.

EXPERIMENTAL PROCEDURES

Experimental Methods

Standard lithography was used to create the microchannel device as previously described in detail (Balzer et al., 2012; Tong et al., 2012). Control or small interfering RNA (siRNA)-treated S180, MDA-MB-231, or CH2879 cells in vehicle control or drug-containing media were added to the cell inlet port of the microchannel device and allowed to migrate into the 3 μm-wide channels in response to a 10% FBS chemoattractant gradient. Cells were then imaged for at least 1 hr using phase-contrast time-lapse microscopy. Then, the media in the appropriate inlets were replaced with (drug- or vehicle-containing) isotonic, hypotonic, or hypertonic media (Figures S2A–S2C) to produce an osmotic shock. In all experiments, the uppermost inlet contained 10% FBS. Phase-contrast time-lapse images were captured again at 3 min intervals for 2 hr.

Cell x,y position within the microchannel was identified as the midpoint between the poles of the cell body (using phase-contrast images) or the nucleus (using fluorescence images of Hoechst-stained cells) and tracked as a function of time. Cell velocity, chemotactic index, and length were

computed as a function of time using a custom-written Matlab program. Instantaneous cell velocity was calculated by dividing each interval displacement by the time interval (3 min), and the mean velocity for a given cell was computed by averaging instantaneous velocities for all time intervals before or after osmotic shock. Chemotactic index was calculated by dividing the end-to-end displacement by the total path length of the cell. Thus, completely directed cell migration resulted in a chemotactic index equal to 1. Cell lengths were measured using the phase-contrast image sequences and the "plot profile" tool in ImageJ to determine the leading and trailing edges of the cell. These measurements were verified by confocal microscopy.

In select experiments, cells were fixed, permeabilized, blocked for nonspecific binding, immunostained for target proteins (NHE-1 and AQP5), and quantitatively analyzed. Statistical significance was determined with a Student's t test or analysis of variance (ANOVA) as appropriate. At least three independent trials were conducted for each experiment, and all data in this article represent the mean ± SEM or SD (as indicated) of pooled data from all experiments. A detailed description of the experimental methods is given in the Extended Experimental Procedures.

Theoretical Methods

The theoretical approach is based on an analysis of hydrostatic and osmotic forces governing water permeation across the cell membrane. In our model, we consider the kinetics of water, kinetics and diffusion of ions, flow of the cell cytoplasm, and mechanics of the cell cortex. Parameters used in our model are listed in Table S1. The detailed theoretical methods and results are described in the Extended Experimental Procedures.

SUPPLEMENTAL INFORMATION

Supplemental Information includes Extended Experimental Procedures, six figures, one table, and one movie and can be found with this article online at http://dx.doi.org/10.1016/j.cell.2014.02.052.

AUTHOR CONTRIBUTIONS

Co-first authors K.M.S. and H.J. contributed equally to this work. K.M.S. and K.K. designed and oversaw all experimental work, and K.M.S. performed most experimental assays and executed all quantitative analyses of experimental data. H.J. and S.X.S. developed the theoretical model, and H.J. fit all data to the theoretical model. S-H.C. established the NHE siRNA assays and associated immunoblots. Z.T. developed the osmolarity assay in the microchannel devices. K.K., S.X.S., and D.W. provided conceptual insight into agreement between the experimental data and the model. K.M.S., H.J., S.X.S., and K.K. wrote the manuscript, which was further edited by all authors. All authors approved the final manuscript.

REFERENCES

Alexander, S., Koehl, G.E., Hirschberg, M., Geissler, E.K., and Friedl, P. (2008). Dynamic imaging of cancer growth and invasion: a modified skin-fold chamber model. Histochem. Cell Biol. 130, 1147–1154.

Atzberger, P.J., Isaacson, S., and Peskin, C.S. (2009). A microfluidic pumping mechanism driven by non-equilibrium osmotic effects. Physica D 238, 1168–1179.

Balzer, E.M., Tong, Z., Paul, C.D., Hung, W.C., Stroka, K.M., Boggs, A.E., Martin, S.S., and Konstantopoulos, K. (2012). Physical confinement alters tumor cell adhesion and migration phenotypes. FASEB J. 26, 4045–4056.

Beltran, A.R., Ramirez, M.A., Carraro-Lacroix, L.R., Hiraki, Y., Reboucas, N.A., and Malnic, G. (2008). NHE1, NHE2, and NHE4 contribute to regulation of cell pH in T84 colon cancer cells. Pflugers Arch. 455, 799–810.

Chae, Y.K., Woo, J., Kim, M.J., Kang, S.K., Kim, M.S., Lee, J., Lee, S.K., Gong, G., Kim, Y.H., Soria, J.C., et al. (2008). Expression of aquaporin 5 (AQP5) promotes tumor invasion in human non small cell lung cancer. PLoS ONE 3, e2162.

Charras, G.T., Yarrow, J.C., Horton, M.A., Mahadevan, L., and Mitchison, T.J. (2005). Non-equilibration of hydrostatic pressure in blebbing cells. Nature 435, 365–369.

Chung, H.J., Jan, Y.N., and Jan, L.Y. (2006). Polarized axonal surface expression of neuronal KCNQ channels is mediated by multiple signals in the KCNQ2 and KCNQ3 C-terminal domains. Proc. Natl. Acad. Sci. USA 103, 8870–8875.

Dreval, V., Dieterich, P., Stock, C., and Schwab, A. (2005). The role of Ca2+ transport across the plasma membrane for cell migration. Cell. Physiol. Biochem. 16, 119–126.

Friedl, P., and Alexander, S. (2011). Cancer invasion and the microenvironment: plasticity and reciprocity. Cell 147, 992–1009.

Goss, G.G., Woodside, M., Wakabayashi, S., Pouyssegur, J., Waddell, T., Downey, G.P., and Grinstein, S. (1994). ATP dependence of NHE-1, the ubiquitous isoform of the Na+/H+ antiporter. Analysis of phosphorylation and subcellular localization. J. Biol. Chem. 269, 8741–8748.

Grinstein, S., Woodside, M., Waddell, T.K., Downey, G.P., Orlowski, J., Pouyssegur, J., Wong, D.C., and Foskett, J.K. (1993). Focal localization of the NHE-1 isoform of the Na+/H+ antiport: assessment of effects on intracellular pH. EMBO J. 12, 5209–5218.

Grunnet, M., MacAulay, N., Jorgensen, N.K., Jensen, S., Olesen, S.P., and Klaerke, D.A. (2002). Regulation of cloned, Ca2+-activated K+ channels by cell volume changes. Pflugers Arch. 444, 167–177.

Hung, W.C., Chen, S.H., Paul, C.D., Stroka, K.M., Lo, Y.C., Yang, J.T., and Konstantopoulos, K. (2013). Distinct signaling mechanisms regulate migration in unconfined versus confined spaces. J. Cell Biol. 202, 807–824.

Iwasaki, T., and Wang, Y.L. (2008). Cytoplasmic force gradient in migrating adhesive cells. Biophys. J. 94, L35–L37.

Jaeger, M., Carin, M., Medale, M., and Tryggvason, G. (1999). The osmotic migration of cells in a solute gradient. Biophys. J. 77, 1257–1267.

Jiang, H.Y., and Sun, S.X. (2013). Cellular pressure and volume regulation and implications for cell mechanics. Biophys. J. 105, 609–619.

Jung, H.J., Park, J.Y., Jeon, H.S., and Kwon, T.H. (2011). Aquaporin-5: a marker protein for proliferation and migration of human breast cancer cells. PLoS ONE 6, e28492.

Keren, K., Yam, P.T., Kinkhabwala, A., Mogilner, A., and Theriot, J.A. (2009). Intracellular fluid flow in rapidly moving cells. Nat. Cell Biol. 11, 1219–1224.

Klein, M., Seeger, P., Schuricht, B., Alper, S.L., and Schwab, A. (2000). Polarization of Na(+)/H(+) and Cl(-)/HCO (3)(-) exchangers in migrating renal epithelial cells. J. Gen. Physiol. 115, 599–608.

Konstantopoulos, K., Wu, P.-H., and Wirtz, D. (2013). Dimensional control of cancer cell migration. Biophys. J. 104, 279–280.

Lang, F., Busch, G.L., Ritter, M., Völkl, H., Waldegger, S., Gulbins, E., and Häussinger, D. (1998). Functional significance of cell volume regulatory mechanisms. Physiol. Rev. 78, 247–306.

Mazzochi, C., Bubien, J.K., Smith, P.R., and Benos, D.J. (2006). The carboxyl terminus of the alpha-subunit of the amiloride-sensitive epithelial sodium channel binds to F-actin. J. Biol. Chem. 281, 6528–6538.

Mingle, L.A., Okuhama, N.N., Shi, J., Singer, R.H., Condeelis, J., and Liu, G. (2005). Localization of all seven messenger RNAs for the actin-polymerization

nucleator Arp2/3 complex in the protrusions of fibroblasts. J. Cell Sci. 118, 2425–2433.

Mitchison, T.J., Charras, G.T., and Mahadevan, L. (2008). Implications of a poroelastic cytoplasm for the dynamics of animal cell shape. Semin. Cell Dev. Biol. 19, 215–223.

Mogilner, A., and Oster, G. (1996). Cell motility driven by actin polymerization. Biophys. J. 71, 3030–3045.

Oster, G.F., and Perelson, A.S. (1987). The physics of cell motility. J. Cell Sci. Suppl. 8, 35–54.

Palamidessi, A., Frittoli, E., Garré, M., Faretta, M., Mione, M., Testa, I., Diaspro, A., Lanzetti, L., Scita, G., and Di Fiore, P.P. (2008). Endocytic trafficking of Rac is required for the spatial restriction of signaling in cell migration. Cell 134, 135–147.

Papadopoulos, M.C., Saadoun, S., and Verkman, A.S. (2008). Aquaporins and cell migration. Pflugers Arch. 456, 693–700.

Pathak, A., and Kumar, S. (2012). Independent regulation of tumor cell migration by matrix stiffness and confinement. Proc. Natl. Acad. Sci. USA 109, 10334–10339.

Pollard, T.D., and Borisy, G.G. (2003). Cellular motility driven by assembly and disassembly of actin filaments. Cell 112, 453–465.

Prentice-Mott, H.V., Chang, C.H., Mahadevan, L., Mitchison, T.J., Irimia, D., and Shah, J.V. (2013). Biased migration of confined neutrophil-like cells in asymmetric hydraulic environments. Proc. Natl. Acad. Sci. USA 110, 21006–21011.

Ritter, M., Schratzberger, P., Rossmann, H., Wöll, E., Seiler, K., Seidler, U., Reinisch, N., Kähler, C.M., Zwierzina, H., Lang, H.J., et al. (1998). Effect of inhibitors of Na+/H+-exchange and gastric H+/K+ ATPase on cell volume, intracellular pH and migration of human polymorphonuclear leucocytes. Br. J. Pharmacol. 124, 627–638.

Schwab, A. (2001). Ion channels and transporters on the move. News Physiol. Sci. 16, 29–33.

Schwab, A., Nechyporuk-Zloy, V., Fabian, A., and Stock, C. (2007). Cells move when ions and water flow. Pflugers Arch. 453, 421–432.

Schwab, A., Fabian, A., Hanley, P.J., and Stock, C. (2012). Role of ion channels and transporters in cell migration. Physiol. Rev. 92, 1865–1913.

Sidhaye, V.K., Chau, E., Srivastava, V., Sirimalle, S., Balabhadrapatruni, C., Aggarwal, N.R., D'Alessio, F.R., Robinson, D.N., and King, L.S. (2012). A novel role for aquaporin-5 in enhancing microtubule organization and stability. PLoS ONE 7, e38717.

Spagnolie, S.E., and Lauga, E. (2010). Jet propulsion without inertia. Phys. Fluids 22, 081902.

Stewart, M.P., Helenius, J., Toyoda, Y., Ramanathan, S.P., Muller, D.J., and Hyman, A.A. (2011). Hydrostatic pressure and the actomyosin cortex drive mitotic cell rounding. Nature 469, 226–230.

Stroka, K.M., Hayenga, H.N., and Aranda-Espinoza, H. (2013). Human neutrophil cytoskeletal dynamics and contractility actively contribute to trans-endothelial migration. PLoS ONE 8, e61377.

Taber, L.A., Shi, Y.F., Yang, L., and Bayly, P.V. (2011). A poroelastic model for cell crawling including mechanical coupling between cytoskeletal contraction and actin polymerization. J. Mech. Mater. Struct. 6, 569–589.

Tong, Z.Q., Balzer, E.M., Dallas, M.R., Hung, W.C., Stebe, K.J., and Konstantopoulos, K. (2012). Chemotaxis of cell populations through confined spaces at single-cell resolution. PLoS ONE 7, e29211.

Wakabayashi, S., Fafournoux, P., Sardet, C., and Pouysségur, J. (1992). The Na+/H+ antiporter cytoplasmic domain mediates growth factor signals and controls "H(+)-sensing". Proc. Natl. Acad. Sci. USA 89, 2424–2428.

Wehner, F., Olsen, H., Tinel, H., Kinne-Saffran, E., and Kinne, R.K. (2003). Cell volume regulation: osmolytes, osmolyte transport, and signal transduction. Rev. Physiol. Biochem. Pharmacol. 148, 1–80.

Wirtz, D., Konstantopoulos, K., and Searson, P.C. (2011). The physics of cancer: the role of physical interactions and mechanical forces in metastasis. Nat. Rev. Cancer 11, 512–522.

Wolf, K., Alexander, S., Schacht, V., Coussens, L.M., von Andrian, U.H., van Rheenen, J., Deryugina, E., and Friedl, P. (2009). Collagen-based cell migration models in vitro and in vivo. Semin. Cell Dev. Biol. 20, 931–941.

Yadav, S., Puri, S., and Linstedt, A.D. (2009). A primary role for Golgi positioning in directed secretion, cell polarity, and wound healing. Mol. Biol. Cell 20, 1728–1736.

Supplemental Information

EXTENDED EXPERIMENTAL PROCEDURES
Osmotic Engine Model

In this paper, we propose a mechanism of cell migration in confined spaces based on directed water permeation. To demonstrate this idea, consider a container partitioned by a semipermeable membrane (Figure 2A, left). Two sides of the partition are connected to reservoirs with constant (but different) solute concentrations. We assume the transport of water through the semipermeable membrane is slow when compared to water diffusion. Therefore, the solute concentrations on the two sides, c_1 and c_2, are spatially uniform. The difference in solute concentrations implies that osmotic pressures on the two sides are different. Osmotic pressure drives the motion of solvent (water) across a semi-permeable membrane from a region of low solute concentration to a region of high solute concentration. This solvent movement tends to decrease the solute concentration difference. Mathematically, the osmotic pressure Π can be estimated using the Van't Hoff equation:

$$\Pi = cRT, \tag{S1}$$

where c is the molar concentration of the solute, R is the gas constant and T is absolute temperature. Suppose the hydrostatic pressures at the two sides are P_1 and P_2, respectively. The net chemical potential of solvent (water) in this situation is a combination of osmotic pressure and hydrostatic pressure. The chemical potentials on the two sides are given by $\Psi_1 = P_1 - \Pi_1$ and $\Psi_2 = P_2 - \Pi_2$. This chemical potential difference drives the flux of water across the semi-permeable membrane. The volume of water passing through a unit area of membrane per unit time can be modeled as proportional to the chemical potential difference: $J = -\alpha(\Psi_2 - \Psi_1)$. At equilibrium when the water flux is zero, the osmotic pressure difference is equal to the hydrostatic pressure difference. However, if the semipermeable membrane can move up and down freely and the motion is so slow that the hydrostatic pressures on the two sides are the same, water molecules will flow to the lower side due to concentration difference ($c_1 < c_2$). Therefore, the membrane moves up at a constant velocity and the velocity is directly determined by the water flux, i.e., $v_0 = J$.

Now let us consider a vesicle enclosed by a semipermeable membrane (Figure 2A, middle). The solute concentrations on the two sides of the vesicle are c_1 and c_3, respectively. The solute concentration is c_2 inside the vesicle. If $c_1 < c_2 < c_3$, then both edges of the vesicle would move upward according to the analysis above. At the steady state, a hydrostatic pressure gradient is developed and maintained so that the water influx at the leading edge is equal to the water efflux at the trailing end. Therefore, the vesicle can move up at a constant velocity. The velocity of the vesicle can be computed from the water flux. To calculate the pressure field, the solvent velocity field inside the cell must be modeled. This detailed calculation will be given in the full model presented in the next section.

Now we consider a living cell migrating in a narrow channel (Figure 2A, right). In a vesicle enclosed by a semipermeable membrane (Figure 2A, middle), the fluxes of solutes and ions are always zero and the flux of water is sufficient to describe motion of the membrane. In contrast, in a "living cell," there are many mechanosensitive (MS) channels and active ion transporters on the cell membrane, which enable the cell to actively control the influx and efflux of ions and other osmolytes. Therefore, the kinetics of the solute must be included in order to study the volume and pressure regulation of a living cell. In our previous work, by considering MS channels and ion transporters, the mechanism of isotropic cell volume and pressure regulation was examined (Jiang and Sun, 2013). In this paper, we consider a model with polarized water and ion transport to understand cell migration in confined spaces. It should be noted that there are multiple species of ions and proteins that can influence osmotic pressure in living cells. In order to simplify this problem, we assume there is only one species of ions.

Kinetics of Water

First, we consider the kinetics of water in a living cell (Figure 2A, right). Suppose the hydrostatic pressure and osmotic pressure inside the cell are $P(x)$ and $\Pi(x)$, respectively. Their boundary values at the upper end and lower end are $P_{in,f}$, $P_{in,b}$, $\Pi_{in,f}$ and $\Pi_{in,b}$. The hydrostatic pressure and osmotic pressure outside the cell are $P_{out,f}$, $P_{out,b}$, $\Pi_{out,f}$ and $\Pi_{out,b}$. Therefore, water chemical potentials inside and outside of the upper end are given by $\Psi_{in,f} = P_{in,f} - \Pi_{in,f}$ and $\Psi_{out,f} = P_{out,f} - \Pi_{out,f}$. Similarly, water chemical potentials inside and outside of the lower end are given by $\Psi_{in,b} = P_{in,b} - \Pi_{in,b}$ and $\Psi_{out,b} = P_{out,b} - \Pi_{out,b}$. The water flux at two ends of the cell are given as

$$\begin{aligned} J_{water,f} &= -\alpha_f(\Psi_{in,f} - \Psi_{out,f}) = -\alpha_f(\Delta P_f - \Delta \Pi_f) \\ J_{water,b} &= -\alpha_b(\Psi_{in,b} - \Psi_{out,b}) = -\alpha_b(\Delta P_b - \Delta \Pi_b) \end{aligned}, \tag{S2}$$

where $\Delta P_f = P_{in,f} - P_{out,f}$, $\Delta P_b = P_{in,b} - P_{out,b}$, $\Delta \Pi_f = \Pi_{in,f} - \Pi_{out,f}$ and $\Delta \Pi_b = \Pi_{in,b} - \Pi_{out,b}$. From the cell volume change we have

$$\frac{dL}{dt} = (J_{water,f} + J_{water,b}), \tag{S3}$$

where L is the length of the cell.

Kinetics of Ions

Beyond the transport of water, we should also consider the kinetics of ion transport in a living cell. The transport of ions is mainly controlled by two types of transmembrane proteins: MS channels and ion transporters. MS channels are membrane proteins that

can open a pore in response to mechanical tension. They act as "emergency valves" to release solutes in response to hypotonic shocks (Kung, 2005). These channels can vary in permeability from nonselective to highly selective for specific anions and cations. They have been found in both prokaryotic and eukaryotic cells. In bacteria, the structure and the mechanisms of MS channels, such as MscS and MscL, have been well studied both experimentally and theoretically. In eukaryotic cells, a large class of proteins called transient receptor potential (TRP) channels, such as TRPV, TRPC, TRPA, TRPP, TRPN and TRPY, have been demonstrated to be mechanosensitive (Kung, 2005). Once the MS channels are open, the flow of ions through the channel is driven by concentration gradients across the membrane.

For a MS channel, the opening probability P_{open} follows a Boltzmann function (Sukharev et al., 1993) (Figure 1B). For N mechanosensitive channels in the cell membrane, there are on average NP_{open} open channels for a given stress. Thus, the ion flux due to the opening of MS channels is proportional to $NP_{open}\Delta c/h_m$, where $\Delta c/h_m$ is the concentration gradient of ions, and h_m is the membrane thickness. We model the MS channel flux as piece-wise linear function of σ, (Jiang and Sun, 2013)

$$J_{out} = \begin{cases} 0 & if & \sigma < \sigma_c \\ -\beta(\sigma - \sigma_c)\Delta\Pi & if & \sigma_c \le \sigma \le \sigma_s \,, \\ -\beta(\sigma_s - \sigma_c)\Delta\Pi & if & \sigma > \sigma_s \end{cases} \tag{S4}$$

where β is a constant. σ_c is the threshold stress below which the ion flux is zero. σ_s is the saturating stress above which all MS channels are open (Jiang and Sun, 2013). In this equation, Δc is substituted by $\Delta\Pi$ since $\Delta\Pi = \Delta cRT$ (Equation S1) and the coefficient RT along with h_m are folded into β. Notice that we use cortical stress σ instead of cortical tension T. Actually, they are related by $T = \sigma h$, where h is the cortical thickness. They are equivalent when the cortical thickness is a constant (Sukharev et al., 1993).

In addition to MS channels, ion transporters actively pump ions against concentration gradients. In order to overcome the energy barrier from an ion concentration or electrochemical gradient, ion transporters utilize energy from ATP hydrolysis, energy releasing enzymatic reactions or light (Jiang and Sun, 2013). For simplicity, we only consider a concentration gradient in this paper. We denote ΔG_a as the free energy input (such as from ATP) during the pumping action. The net free energy change during the pumping action is therefore $\Delta G = RT \log(c_{in} - c_{out}) - \Delta G_a$, where c_{in} and c_{out} are the ion concentration inside and outside the cell, respectively. In most cases, $c_{in} > c_{out}$ and the first term of ΔG is positive. Therefore, energy input ΔG_a is required. The critical ion concentration, $c_{in,c} = c_{out} \exp(\Delta G_a/RT)$, is obtained by setting $\Delta G = 0$. The critical concentration is the concentration above which energy from ATP is insufficient for ion transporters to pump ions against the concentration gradient. Therefore, the influx of ions from active pumping of ion transporters can be described by

$$J_{in} = \gamma(\Delta\Pi_c - \Delta\Pi), \tag{S5}$$

where γ is a rate constant. When $\Delta\Pi$ is larger than $\Delta\Pi_c$, note that the flux can be negative. The free energy from a mole of ATP during typical cellular conditions is about 30 kJ, which yields $c_{in,c} \approx 6 \times 10^4 c_{out}$ for an ion transporter driven by ATP hydrolysis. The osmotic pressure of the growth medium used in our experiment is about $\Pi_{out} = 0.88\,MPa$, and a critical osmotic pressure difference $\Delta\Pi_c = \Pi_{out}[\exp(\Delta G_a/RT) - 1] \approx 6 \times 10^4 \Pi_{out} \approx 5.4 \times 10^4 MPa$. It should also be noted that this kind of active transport is a complex process, involving multistep enzyme reactions (Pont and Bonting, 1981). The expression and activity of ion transporters may be controlled by other regulators or ATP/ADP concentration (Pont and Bonting, 1981).

Given the influx and efflux of ions, the change in the total number of ions inside the cell is therefore given by

$$\frac{dn}{dt} = S(J_{in,f} + J_{out,f} + J_{in,b} + J_{out,b}), \tag{S6}$$

where S is the area of the cross-section of the narrow channel. Notice that influx is positive and efflux is negative (Equations S4 and S5).

Flow of Cytoplasm

Following Ref. (Hawkins et al., 2009), we model the cytoplasm of the cell as a viscous fluid and assume that the width of the channel b is much smaller than cell length. Therefore, we can use lubrication theory, which describes the flow of fluids in geometries where one dimension is significantly smaller than the others. We obtain a leading-order approximation of the Stokes equations. By using lubrication approximation, the flow of cytoplasm can be solved from

$$\frac{\partial P}{\partial y} = \frac{\partial P}{\partial z} = 0$$
$$\frac{\partial P}{\partial x} = \eta \frac{\partial^2 v}{\partial z^2} \tag{S7}$$

where P is the pressure, η is the viscosity of the cytoplasm, and $v(z)$ is the velocity field of the cytoplasm. Boundary conditions of cytoplasm are $v = v_0$ at $z = 0$ and $z = b$, where v_0 is the cell migration speed. By solving Equation S7, the velocity field is $v(z) = (1/2\eta)(\partial P/\partial x)(z^2 - bz) + v_0$. The average velocity of the cytoplasm can be given as $\overline{v} = 1/b \int_0^b v(z)dz = -(b^2/12\eta)(\partial P/\partial x) + v_0$, which should be zero in our problem. Therefore, we obtain

$$v_0 = \frac{b^2}{12\eta}\frac{\partial P}{\partial x}. \tag{S8}$$

By solving this equation, we can find $P(x) = P_{in,b} + (12\eta/b^2)v_0 x$, where $P_{in,b}$ is the hydrostatic pressure at the trailing end. Therefore, the hydrostatic pressure at the leading end is $P_{in,f} = P_{in,b} + (12\eta/b^2)v_0 L$. If we consider the hydrostatic pressure difference, we have $\Delta P_f = \Delta P_b + (12\eta/b^2)v_0 L + (P_{out,b} - P_{out,f})$, where $\Delta P_f = P_{in,f} - P_{out,f}$ and $\Delta P_b = P_{in,b} - P_{out,b}$. In our experiments, the hydrostatic pressure difference between the two sides of the channels is very small (at most several Pascals) compared to the osmotic shocks applied (several hundred kiloPascals). Therefore, we can assume $P_{out,f} = P_{out,b}$ and rule out the possibility that the cell is pushed by a hydrostatic pressure difference.

Force Balance and Constitutive Law of the Cortical Layer

By considering the force balance of a thin slice of the cortex perpendicular to the migration direction, we obtain the force balance equation of the cortical layer as $[T(x + dx) - T(x)]w = \eta\partial v/\partial z|_{z=b}wdx + \xi_w v_0 wdx$, where w is the height of the channel and T is the cortical tension. The cortical stress is thus given by $\sigma = T/h$. Here, $\eta\partial v/\partial z|_{z=b}wdx$ is the viscous drag force from the cytoplasm; $\xi_w v_0 wdx$ is the friction force between the cell and the channel wall, and ξ_w is the friction coefficient. Notice that from the symmetry of our problem, we only consider the force balance of the cortical layer at $z = b$. Then, the above equation can be simplified as

$$\frac{\partial T}{\partial x} = \left(\frac{6\eta}{b} + \xi_w\right)v_0. \tag{S9}$$

The boundary condition is $T = T_b = \Delta P_b b/2$ at the trailing end. So $T(x) = \Delta P_b b/2 + ((6\eta/b) + \xi_w)v_0 x$ and the cortical tension at the leading end is $T_f = \Delta P_b b/2 + (6\eta/b + \xi_w)v_0 L = \Delta P_f b/2 - (P_{out,b} - P_{out,f}) + \xi_w v_0 L$.

We use the simplest viscoelastic constitutive law for the cell cortex

$$\sigma = E_c\left(\lambda^{1/m} - 1\right) + \eta_c\frac{d\lambda}{dt} - \sigma_a, \tag{S10}$$

where $\lambda = dx/dX$, m is an integer, X and x are the coordinates before and after the deformation of cortex. E_c and η_c are the elastic modulus and viscosity of the material, respectively. σ_a is the active stress due to the contraction of myosin motors. Notice that σ_a is negative since myosin applies a contractile force on the actin filament network. Equation S10 can be reduced to the classic Kelvin-Voigt model when $m = 1$ and the strain is small. In this paper, we are interested in the steady state of the system. Therefore, $d\lambda/dt = 0$. Using the relation $T = \sigma h$ and the solution to Equation S9, we have

$$L_0 = \begin{cases} \dfrac{1}{A_2}\log\left[\dfrac{A_1 + A_2 L}{A_1}\right] & m = 1 \\[2em] \dfrac{1}{(m-1)A_2}\left[\dfrac{1}{A_1^{m-1}} - \dfrac{1}{(A_1 + A_2 L)^{m-1}}\right] & m > 1 \end{cases}, \tag{S11}$$

where $A_1 = (E_c h + \sigma_a h + \Delta P_b b/2)/(E_c h)$, $A_2 = ((6\eta/b + \xi_w)v_0)/E_c h$, and L_0 and L are the cell lengths before and after deformation. Therefore, L_0 can be calculated easily once the cell migration speed v_0 is obtained.

Notice that the contribution of the active stress to the migration speed and cell volume is negligible if $|\sigma_a/E_c| \ll 1$, since σ_a only appears in the expression of A_1. This is the case we found in our experiments, with no change in migration velocity for S180 cells treated with 50 μM blebbistatin (Figure 1A).

Diffusion of Ions inside the Cell

To simplify the problem, we assume that ions freely diffuse inside the cell. Therefore, we have

$$\frac{\partial c_{in}}{\partial t} + \mathbf{v} \cdot \nabla c_{in} = D\nabla^2 c_{in}, \tag{S12}$$

where c_{in} is the ion concentration inside the cell, D is the diffusion constant, and $\mathbf{v} = (v, 0, 0)$ is the velocity of the cytoplasm. Notice that in our experiment the typical migration speed is tens of micron per hour, which is much slower than the diffusion of ions.

Therefore, the Péclet number is very low and the convection term $\mathbf{v} \cdot \nabla c_{in}$ can be neglected in Equation S12. We further assume that the ion concentration is only the function of x. Therefore, in steady state $(\partial c_{in}/\partial t = 0)$, we obtain $c_{in}(x) = c_{in,b}(1 - x/L) + c_{in,f} x/L$, where $c_{in,f}$ and $c_{in,b}$ are the ion concentrations at the leading and trailing ends, respectively. Thus, the osmotic pressure is given by $\Pi_{in,f} = RTc_{in,f}$ and $\Pi_{in,b} = RTc_{in,b}$ from the Van't Hoff equation (Equation S1). Then, the diffusive ion flux inside the cell is simply given as $-D\nabla c_{in} = -D(c_{in,f} - c_{in,b}/L)$.

At steady state, $dn/dt = 0$ and the absolute value of the ion flux at the leading and tailing ends should be equal to the diffusive ion flux inside the cell. Therefore, we have

$$J_{in,f} + J_{out,f} = D\frac{c_{in,f} - c_{in,b}}{L}$$
$$J_{in,b} + J_{out,b} = -D\frac{c_{in,f} - c_{in,b}}{L}. \tag{S13}$$

Similarly, at steady state, $dL/dt = 0$ and the absolute value of water flux at the leading and trailing ends should be equal to the cell migration speed. Therefore,

$$J_{water,f} = v_0$$
$$J_{water,b} = -v_0. \tag{S14}$$

By solving the coupled Equations S8, S9, S12, S13, and S14, we can obtain the cell migration speed v_0 at steady state. These governing equations are nonlinear. If we solve the full nonlinear equations numerically, we can find four solutions. However, three of them are unphysical since the cortical stress is negative at least on one edge of the cell. In order to obtain some insights of the migration velocity without losing generality, we can linearize the equations by eliminating the $\Delta \Pi$ term in Equation S4. In this case, we obtain an analytical solution for the migration speed:

$$v_0 = \frac{b^2 h\alpha\{2D(\Pi_{out,b} - \Pi_{out,f}) + LRT[\gamma(\Delta\Pi_{c,f} - \Delta\Pi_{c,b}) + \beta(\sigma_{c,f} - \sigma_{c,b})]\}}{6bL^2 RT\alpha\beta\eta + 12hL\alpha\eta(2D + LRT\gamma) + b^2[4Dh + LRT(2h\gamma + L\alpha\beta\zeta_w)]}. \tag{S15}$$

If the cell is uniform (all parameters are uniform inside the cell), the speed is zero. However, if the cell is polarized, i.e., the critical values of the MS channels and ion pumps ($\Delta\Pi_{c,f}$, $\Delta\Pi_{c,b}$, $\sigma_{c,f}$ and $\sigma_{c,b}$) are different at the leading and trailing edges, or the distributions of the MS channels and ion pumps (β_f, β_b, γ_f, and γ_b) are different at the leading and trailing edges, then we obtain a nonzero migration speed. This is consistent with the idea that cell migration requires the polarization of the cell. In Equation S15, to simplify the formula we have assumed that the rate constants α, β, and γ are the same at the two ends of the cell. The general solution where α, β, and γ are different at the leading and trailing ends is not given here since the equation is simply too long.

Note that Equation S15 only depends on the current cell length, L, and is independent of the details of cortical mechanics. The cortical mechanics determines the relationship between the reference length, L_o, and the apparent length, L. However, the migration speed does not depend on this difference. In addition, the migration velocity is only weakly dependent on the length of the cell (see Figure S4). This could explain why actomyosin inhibition does not affect cell velocity in S180 cells; the cell volume changes when actin and myosin are inhibited (data not shown). However, the migration speed is essentially the same.

The model results predict that if cells migrate in narrow channels using this "osmotic engine" mechanism, then osmotic shocks must strongly influence the cell migration velocity. Therefore, from Equation S15, we can see if we decrease the osmotic pressure outside the cell $\Pi_{out,f}$, the sign of the migration speed could change. It should be noted that $\Delta\Pi_{c,f} \propto \Pi_{out,f}$ and $\Delta\Pi_{c,b} \propto \Pi_{out,b}$ as discussed above. $\Delta\Pi_{c,f}$ and $\Delta\Pi_{c,b}$ could also change when osmotic shocks are applied. For estimated parameters for real cells, our model predicts that hypotonic shock at the leading edge of the cell can lead to reversal of the cell. Similarly, the cell can also reverse direction if we increase $\Pi_{out,b}$(hypertonic shock at the trailing edge). The model predicts that hypotonic shock at the leading edge is equivalent to the hypertonic shock at the trailing edge. Both of the shocks can potentially reverse the cell migration direction. This prediction is not very intuitive, but is testable. Indeed, our experiments completely verified this prediction. The comparison between numerical results and experimental results is shown in Figure 3.

In our model, each cell has a constant reference length C_0. The reference length of the cell may be established by other mechanical elements in the cell such as microtubules and intermediate filaments. By calculating the migration velocity (Equation S15) and the current cell length (Equation S11), we can obtain L_o for each L. By minimizing the error function $(L_0 - C_0)^2$, we can determine the corresponding migration velocity and current cell length for a fixed reference length C_0. Using this method, we find that cell volume or cell length decreases after the hypotonic shock is applied at the leading edge. This is quite counterintuitive since the volume of a lipid vesicle should increase after a hypotonic shock. The reason is that $\Delta\Pi_c$ is linearly proportional to Π_{out} as we have discussed earlier. This means osmotic shocks can also influence the ability of ion transport through ion pumps. This prediction is nontrivial and it is also testable. In the experiments, we did find that cell length decreased after the hypotonic shock was applied at the leading edge (Figure 4). This prediction is also valid for the hypotonic shock at the trailing end.

We found that the migration speed increases as the channel width increases. This prediction is consistent with the previous experimental observation (Irimia and Toner, 2009). We also found that the migration speed depends on the cell volume, i.e., big cells

migrate slower. In reality, the variation in cell volume is quite large even for a single cell type. Therefore, there should also be a distribution of migration speed in the experiments. Figure S4 shows the plot of migration speed before and after osmotic shocks are applied on the leading edge and trailing edge.

Parameters Used in the Model

The parameters used in our model are summarized in Table S1. The thickness of the cortex is less than 1 μm (Pesen and Hoh, 2005; Tinevez et al., 2009). The elastic modulus of the cortex is about several kPa (Kuznetsova et al., 2007). The diffusion constants of ions inside the cytoplasm are slightly smaller than that in water (about $10^3 \mu m^2/s$) (Edzes and Berendsen, 1975). So we use $500 \mu m^2/s$ in the calculation. The viscosity of the cytoplasm is similar to the viscosity of water ($0.001\ Pa \cdot s$) (Luby-Phelps, 2000). The friction force applied by the channel wall should be around several nN (Raman et al., 2013). The contact area between the cell and the channel wall is about $(10 + 10 + 3 + 3) \times 60\ \mu m^2$ if the cell length is 60 μm. The cell migration speed is about $10^1 \mu m/hour$. Therefore the friction coefficient (the friction force per unit area per unit velocity) between the cell and channel wall is estimated to be $10^8 \sim 10^9 Pa \cdot s/m$. In eukaryotic cells, the threshold tension of the mechanosensitive channels T_c is much lower than that of mechanosensitive channels in prokaryotic cells ($12 dyn/cm$ for MscL channels in *E. coli*) (Kung, 2005). We are studying eukaryotic cells in this paper. Therefore, we estimate a small threshold stress $\sigma_c = 900\ Pa$ for MS channels here. The saturating stress of MS channel σ_s is assumed to be three times its threshold stress. Across various eukaryotic cells, the permeability rate P_f is usually reported in the range $10^{-5} \sim 10^{-4} m/s$ (Marrink and Berendsen, 1994). The definition of the water permeability rate relates the flux created by a concentration $J = P_f V_w \Delta c = (P_f V_w/RT) \Delta \Pi$, where V_w is the molar volume of water, Δc is the difference of concentration across the membrane, and $\Delta \Pi$ is the osmotic pressure difference across the membrane. Therefore, from this relation we obtain $\alpha = P_f V_w/RT$, which suggests that $\alpha = 10^{-13} \sim 10^{-12} m \cdot Pa^{-1} \cdot s^{-1}$. The rate constants β and γ can be regarded as fitting parameters in this model.

Ruling out a Suction-Driven Mechanism of Cell Migration

Our experimental and theoretical results align to support a mechanism of cell migration that is based on directed water permeation in confined spaces. We would like to note that in our microchannel device, the height of media in all inlets (for cells and media) was the same; thus, there was no hydrostatic pressure difference between the top and bottom of the channel, leading to constant and equal flows in the large media channel and cell seeding channel perpendicular to the 3 μm channels. Therefore, it is not possible that the cells are simply being suctioned through the narrow channels by hydrostatic pressure. In most experiments, not all channels contain cells, which would not be the case if a suction force were driving them into and across the channels. The suction hypothesis also cannot explain the reversal of cell migration after a hypotonic shock at the leading edge. Furthermore, we have shown that in fibroblast cells, inhibition of myosin II via blebbistatin (i.e., decreasing cell stiffness) decreases migration speed (Hung et al., 2013), in contrast to tumor cells. If suction were driving cell migration, blebbistatin treatment would increase cell migration speed in these experiments.

To experimentally verify that cells were not being suctioned across the channels, we performed two experiments. First, we allowed cells to enter into and migrate across microchannels in the absence of a chemoattractant gradient. Cell migration speed and chemotactic index were significantly decreased in the absence of a chemoattractant gradient, in comparison with a 10% FBS gradient (Figures S6E and S6F). This indicates that cells are responding to the chemoattractant gradient (which presumably helps the cell to set up the appropriate polarization of ion pumps), rather than being driven by a suction force. In the second experiment, cells were allowed to migrate into the channels in response to a 10% FBS gradient (with equal volume heights in the inlets but with no media to start in the outlets), but once the cells were in the channels, all inlets *and* outlets were replaced with equal heights of media, thus eliminating all media flow within the device. If a suction force were driving cell migration, this removal of flow would stop cell migration. However, we observed no difference in cell migration speed after removal of flow (Figure S6E). Hence, there is no suction force driving cell migration in the microfluidic channels; rather our results strongly support a paradigm based on directed water permeation through the cell membrane. We would also like to point out that migration speeds were not different in 4-walled PDMS channels, in comparison with 3 walls PDMS and the bottom surface glass used in the majority of our experiments (Figure S6E), indicating that the two situations produce identical results.

Cell Lines and Reagents

S180 sarcoma cells (generous gift from Dr. Jean Paul Thiery, A Star, Institute of Molecular and Cellular Biology, Singapore) and MDA-MB-231 metastatic breast cancer cells (American Type Culture Collection, Manassus, VA, USA) were cultured in DMEM (GIBCO, Grand Island, NY, USA) supplemented with 10% fetal bovine serum (FBS; GIBCO) and 1% penicillin/streptomycin (100 units penicillin, 100 μg/ml streptomycin). CH2879 chondrosarcoma cells (generous gift from Dr. Antonio Llombart-Bosch, University of Valencia, Spain) were cultured in RPMI (GIBCO) supplemented with 10% FBS and 1% antibiotic-antimycotic (Life Technologies, Grand Island, NY, USA). Cells were maintained in a humidified incubator at 37°C, 5% CO₂/95% air. During select migration assays, culture medium was supplemented with the following pharmacological drugs (each from Sigma-Aldrich, St. Louis, MO, USA): blebbistatin (50 μM), Lat-A (2 μM), nocodazole (16.6 μM), 5-(N-Ethyl-N-isopropyl)amiloride (EIPA; 10, 20, or 50 μM) or vehicle control (≤0.1% dimethylsulfoxide or EtOH). To knockdown NHE-1, cells were transiently transfected with NHE-1 siRNA (Santa Cruz Biotechnology, Santa Cruz, CA, USA) via Lipofectamine 2000 (Life Technologies), according to the manufacturer's protocol. To knockdown AQP5, cells were infected with an adenovirus containing AQP5 siRNA, which was received as a generous gift from the lab of Dr. Ramana Sidhaye (Pulmonary and Critical Care Medicine, Johns Hopkins University School of Medicine). The adenovirus was added to the apical surface of confluent cells in a 6-well plate and cells were "spinoculated" for 5 min at 700 rpm and 4°C using a bench top centrifuge. AQP5 was successfully knocked down 5 days after spinoculation, at which point all experiments (migration assays and western

blots) were conducted. Knockdown efficiency and expression of sodium hydrogen exchangers and AQPs was measured via western blotting with the following antibodies, which were all purchased from Santa Cruz Biotechnology: NHE-1 (sc-16097), NHE-2 (sc-22928), NHE-4 (sc-16104), AQP1 (sc-9878), AQP3 (sc-9885), and AQP5 (sc-9890), and compared to an internal control (Sigma, anti-β-actin; A5441).

Fabrication of Microfluidic Devices

Standard lithography was used to create the microchannel device as previously described in detail (Balzer et al., 2012; Tong et al., 2012). Briefly, a 10 μm-thick layer of SU-8 photoresist (MicroChem Corporation, Newton, MA, USA) was spin-coated onto a silicon wafer and cross-linked by UV light exposure through a photomask with variable transparent separation distances, ranging from 3 μm to 50 μm (the width of the final microchannels in the device). Developer was used to remove non-crosslinked photoresist. Next, a 50 μm-thick layer of SU-8 photoresist was spin-coated onto the silicon wafer, followed by exposure to UV light through a second mask containing two 400 μm-wide channels spaced 200 μm apart (the dimensions of the cell and media inlet ports in the final device). Developer was again used to remove non-crosslinked photoresist from the second feature. Polydimethylsiloxane (PDMS) was prepared at a 10:1 ratio with the curing agent, poured over the silicon master, and degassed in a vacuum chamber for 2 hr. The PDMS was baked at 85°C for 1 hr, peeled off the master, cut to appropriate size, and pierced to form inlet and outlet ports. The PDMS device and 75 mm glass coverslip were treated with oxygen plasma for 3 min and irreversibly sealed together upon contact, forming 4-walled microchannels of width determined by the first feature created by photolithography. In select experiments, a thin layer of de-gased PDMS was spin-coated onto the glass coverslip, and both the microfluidic device and PDMS-coated coverslip were plasma treated and bound together, forming 4-walled PDMS microchannels. The surface of the PDMS microchannels was functionalized by adding type-1 collagen or fibronectin (both at 20 μg/ml in PBS) to the ports of the device and incubating for 1 hr at 37°C.

Microchannel Seeding and Live-Cell Imaging

Cells were trypsinized, resuspended in serum-containing medium to neutralize the trypsin, and subsequently washed in serum-free media. In select experiments to track the cell nucleus, cells were incubated with 1:5000 Hoechst (Life Technologies) in serum-free medium for 15 min, centrifuged, resuspended in serum-free medium to wash, centrifuged again, and finally resuspended in serum-free medium. A 25 μl cell suspension (1 × 10^5 cells total) was added to the cell inlet port, and cells were transported along the seeding channel by pressure-driven flow. Within 5 min the cell suspension was removed and replaced with 50 μl of serum-free medium, which was also added to the upper inlets. Serum-containing media was added to the top-most inlet port, thus forming a chemoattractant gradient by diffusion across the laminar flow. Media added to all ports contained either select drugs or the vehicle control. For Lat-A treatment only, medium-containing drug was added after the cells had mostly entered the channels. Chambers were placed in an enclosed, humidified microscope stage at 5% CO_2 and 37°C (TIZ, Tokai Hit Co., Japan). Phase contrast time-lapse images were captured at 3 min intervals for 1 hr before osmotic shock using an inverted Nikon microscope with a 10×/0.45 NA Ph1 objective at multiple stage positions via stage automation (Nikon Elements, Nikon, Japan). Hoechst-stained cells were tracked every 6 min to reduce exposure to fluorescent light during live-cell imaging.

Osmotic Shock Assays

Hypotonic solutions were prepared by adding varying amounts of filtered, deionized water to DMEM (Figure S2D). Hypertonic solutions were prepared by adding xylose (0.5%, 1%, 2%, or 4%) to DMEM. The osmolarity of each solution was measured using freezing point depression with an Advanced Instruments Micro-Osmometer (Norwood, MA, USA). After 1 hr of live cell imaging in isotonic media, the media in the appropriate inlets was replaced with (drug- or vehicle-containing) isotonic, hypotonic, or hypertonic media (Figures S2A–S2C). In all experiments, the uppermost inlet contained 10% FBS. Note that media in all wells was refreshed, even if isotonic media was added. This exchange required approximately 5 min to complete, including time to stabilize the coverslip after adding new media and to refocus the microscope in all imaging locations. Phase contrast time-lapse images were captured again at 3 min intervals for 2 hr. Cell velocity, chemotactic index, and length were computed as a function of time. In select experiments, cells were fixed, permeabilized, blocked for nonspecific binding, immunostained for target proteins, and quantitatively analyzed, as described below.

FITC-Dextran Assays

To confirm that cells completely occlude the channels (Hung et al., 2013), we introduced FITC-dextran (0.6 μg/ml in cell culture medium) into the top inlets of devices containing cells within the channels, while medium in the bottom inlet of the device was refreshed with regular medium. Following addition of the FITC-dextran, confocal images were captured at 15 min intervals using a Zeiss LSM 700 laser scanning confocal microscope (Carl Zeiss MicroImaging, Thornwood, NY, USA) and a 63×/1.4 NA oil objective and Zen Black software.

Analysis of Cell Migration, Length, and Volume

Cell x,y position within the microchannel was identified as the midpoint between the poles of the cell body (using phase contrast images) or the nucleus (using fluorescence images of Hoechst-stained cells) and tracked as a function of time using ImageJ (NIH, Bethesda, MD, USA). Cells were only analyzed if no other cell was in the same channel or entering the channel. Cell velocity and chemotactic index were computed using a custom-written Matlab (The MathWorks, Natick, MA, USA) program. Instantaneous cell velocity was calculated by dividing each interval displacement by the time interval (3 min), and the mean velocity for a given cell was computed by averaging instantaneous velocities for all time intervals before or after osmotic shock. Importantly, migration velocities computed using 3, 6, or 9 min intervals were identical (data not shown) and therefore we chose to use 3 min in order to provide the best time resolution. Negative velocities indicated a change in direction of migration. Chemotactic index was calculated by dividing the end-to-end displacement by the total path length of the cell. Thus, completely directed cell migration resulted in a

chemotactic index equal to 1. The reported velocity and chemotactic index for each condition is the mean of the pooled cells from at least three independent experiments. Cell lengths were measured using the phase-contrast image sequences and the "plot profile" tool in ImageJ to determine the leading and trailing edges of the cell. Cell volume in suspension was calculated using the diameter of the projection of spherical cells in suspension above a bovine serum albumin-coated substrate, with isotonic, hypotonic, or hypertonic medium.

Immunofluorescence

Cells within the microchannels were fixed in 3.7% formaldehyde (Fisher Scientific, Pittsburgh, PA, USA) for 10 min, permeabilized in 0.5% Triton X-100 (Sigma-Aldrich) for 5 min, and blocked for nonspecific binding in 2.5% bovine serum albumin (BSA; Sigma-Aldrich) for 1 hr at ambient temperature. Cells were washed three times with PBS in between each step. Primary antibody solutions were then added according to the following specifications: AQP5 (1:100; Santa Cruz Biotechnology sc-9890) or NHE-1 (1:100; Santa Cruz Biotechnology sc-16097) for 1 hr at ambient temperature. Cells were washed again three times with PBS and incubated for 1 hr at ambient temperature in the appropriate secondary solutions: Alexa Fluors (488, 568 or 633; Life Technologies) conjugated to α-goat IgG (1:100), Alexa-conjugated phalloidin (1:500, Molecular Probes, Grand Island, NY, USA), and Hoechst 33342 (1:5000; Sigma-Aldrich). Cells were imaged using a Zeiss LSM 510 META laser scanning confocal microscope (Carl Zeiss MicroImaging) and a 63×/1.4 NA oil objective and LSM software (version 4.2). For quantification of NHE-1 and AQP5 localization in each cell, the following sequence was performed: (1) the confocal image stack was integrated into a single image; (2) the cell boundary was identified and boxed; (3) the "plot profile" command in ImageJ was applied to create a list of average intensities for each line of pixels along the length of the cell; (4) a custom-written Matlab code was used to break up the cell into 20 segments, average the intensity values for each segment, normalize the intensity values to the maximum intensity for that cell, and normalize the segment's distance from the trailing end to the total length of the cell; and (5) normalized fluorescence intensity was plotted as a function of normalized distance from the cell's trailing edge. To confirm western blotting results for expression of sodium hydrogen exchangers and AQPs, immunofluorescence was performed using a similar procedure. Cells were plated onto 2D glass coverslips, allowed to spread overnight, fixed, permeabilized, blocked, stained with primary antibodies (same as for western blotting procedure described above) at 1:100 dilution for 2 hr at ambient temperature, and stained with secondary antibody (Alexa Fluor 633) at 1:100 dilution for 1 hr at ambient temperature. Imaging was performed, as above, with a confocal microscope. The average fluorescence intensity for 25–45 cells per condition was measured using ImageJ.

Statistical Methods

Statistical significance was determined between sample means using a student's t test or between groups using ANOVA followed by individual post-hoc comparisons via Tukey tests. Statistical tests were done either in Excel (Microsoft Corporation) or in Matlab. At least three independent trials were conducted for each experiment, and all data in this article represent the mean ± SEM (or SD, as indicated) of pooled data from all experiments.

SUPPLEMENTAL REFERENCES

Balzer, E.M., Tong, Z., Paul, C.D., Hung, W.C., Stroka, K.M., Boggs, A.E., Martin, S.S., and Konstantopoulos, K. (2012). Physical confinement alters tumor cell adhesion and migration phenotypes. FASEB J. *26*, 4045–4056.

Edzes, H.T., and Berendsen, H.J. (1975). The physical state of diffusible ions in cells. Annu. Rev. Biophys. Bioeng. *4*, 265–285.

Hawkins, R.J., Piel, M., Faure-Andre, G., Lennon-Dumenil, A.M., Joanny, J.F., Prost, J., and Voituriez, R. (2009). Pushing off the walls: a mechanism of cell motility in confinement. Phys. Rev. Lett. *102*, 058103.

Hung, W.C., Chen, S.H., Paul, C.D., Stroka, K.M., Lo, Y.C., Yang, J.T., and Konstantopoulos, K. (2013). Distinct signaling mechanisms regulate migration in unconfined versus confined spaces. J. Cell Biol. *202*, 807–824.

Irimia, D., and Toner, M. (2009). Spontaneous migration of cancer cells under conditions of mechanical confinement. Integr. Biol. (Camb.) *1*, 506–512.

Jiang, H.Y., and Sun, S.X. (2013). Cellular pressure and volume regulation and implications for cell mechanics. Biophys. J. *105*, 609–619.

Kung, C. (2005). A possible unifying principle for mechanosensation. Nature *436*, 647–654.

Kuznetsova, T.G., Starodubtseva, M.N., Yegorenkov, N.I., Chizhik, S.A., and Zhdanov, R.I. (2007). Atomic force microscopy probing of cell elasticity. Micron *38*, 824–833.

Luby-Phelps, K. (2000). Cytoarchitecture and physical properties of cytoplasm: volume, viscosity, diffusion, intracellular surface area. Int. Rev. Cytol. *192*, 189–221.

Marrink, S.J., and Berendsen, H.J.C. (1994). Simulation of water transport through a lipid-membrane. J. Phys. Chem. *98*, 4155–4168.

Pesen, D., and Hoh, J.H. (2005). Micromechanical architecture of the endothelial cell cortex. Biophys. J. *88*, 670–679.

Pont, J.J.H.H.M.d., and Bonting, S.L. (1981). Membrane Transport (Amsterdam: Elsevier/North-Holland Biomedical Press).

Raman, P.S., Paul, C.D., Stroka, K.M., and Konstantopoulos, K. (2013). Probing cell traction forces in confined microenvironments. Lab Chip *13*, 4599–4607.

Sukharev, S.I., Martinac, B., Arshavsky, V.Y., and Kung, C. (1993). Two types of mechanosensitive channels in the Escherichia coli cell envelope: solubilization and functional reconstitution. Biophys. J. *65*, 177–183.

Tinevez, J.Y., Schulze, U., Salbreux, G., Roensch, J., Joanny, J.F., and Paluch, E. (2009). Role of cortical tension in bleb growth. Proc. Natl. Acad. Sci. USA *106*, 18581–18586.

Tong, Z.Q., Balzer, E.M., Dallas, M.R., Hung, W.C., Stebe, K.J., and Konstantopoulos, K. (2012). Chemotaxis of cell populations through confined spaces at single-cell resolution. PLoS ONE *7*, e29211.
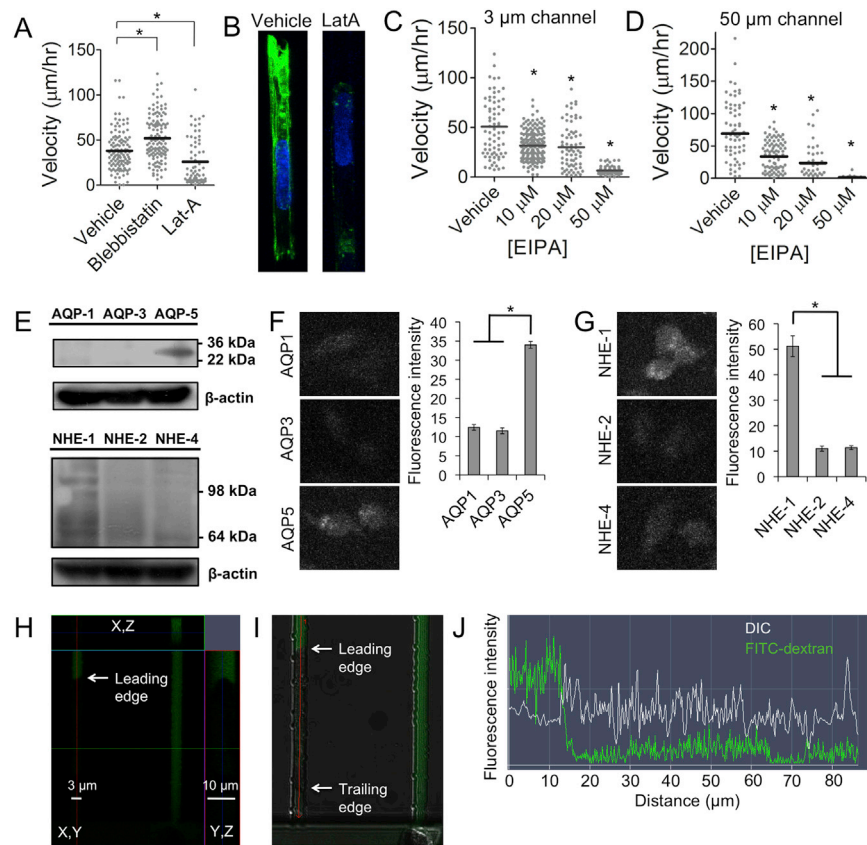
Figure S1. Role of Actin, Myosin, and Na⁺/H⁺ Exchangers in Confined Migration of MDA-MB-231 Cells, Related to Figure 1

(A) MDA-MB-231 cell velocity in the presence of 50 μM blebbistatin or 2 μM Lat-A. Each data point represents average velocity of one cell over the course of 2 hr. Horizontal bars indicate mean.

(B) Confocal images of vehicle control- or LatA-treated MDA-MB-231 cells stained for actin (green) by phalloidin-Alexa488 and the nucleus (blue) by Hoechst.

(C and D) Velocity (C) and chemotactic index (D) of MDA-MB-231 cells treated with increasing concentrations of EIPA. All migration experiments were performed in 3 μm-wide channels.

(E–G) Also shown are (E) immunoblots and (F and G) immunostained images (taken using identical detector voltage, scan speed, pixel resolution, and laser power) demonstrating expression levels of AQPs and Na⁺/H⁺ exchangers in S180 cells. Two cells are shown in each of the immunostained images and Hoechst staining (not shown) was used to detect presence of cells. White scale bars represent 20 μm in (F) and (G). Quantification of fluorescence intensity in 25–45 S180 cells, depending on condition, is shown for (F) AQPs and (G) Na⁺/H⁺ exchangers.

In (A), (C), and (D), * indicates p < 0.05 in comparison with vehicle control by Student's t test. In (F) and (G), * indicates p < 0.05 by ANOVA followed by Tukey test.

(H) Confocal orthogonal image (at t = 60 min) of FITC-dextran, which was introduced into the upper inlets at t = 0. The Z,Y cross-sectional plane demonstrates that the FITC-dextran does not move past the leading edge of the cell.

(I) DIC and fluorescence confocal slices of images showing (left) a 3 μm-wide channel occupied by a cell and (right) a 3 μm-wide empty channel. The leading and trailing edges of the cell are visible in the DIC image and are indicated with white arrows.

(J) Fluorescence and DIC intensities as a function of distance along the middle of the channel in panel I (left). The leading edge of the cell is indicated at a distance of approximately 13 μm, where FITC-dextran intensity sharply decreases.
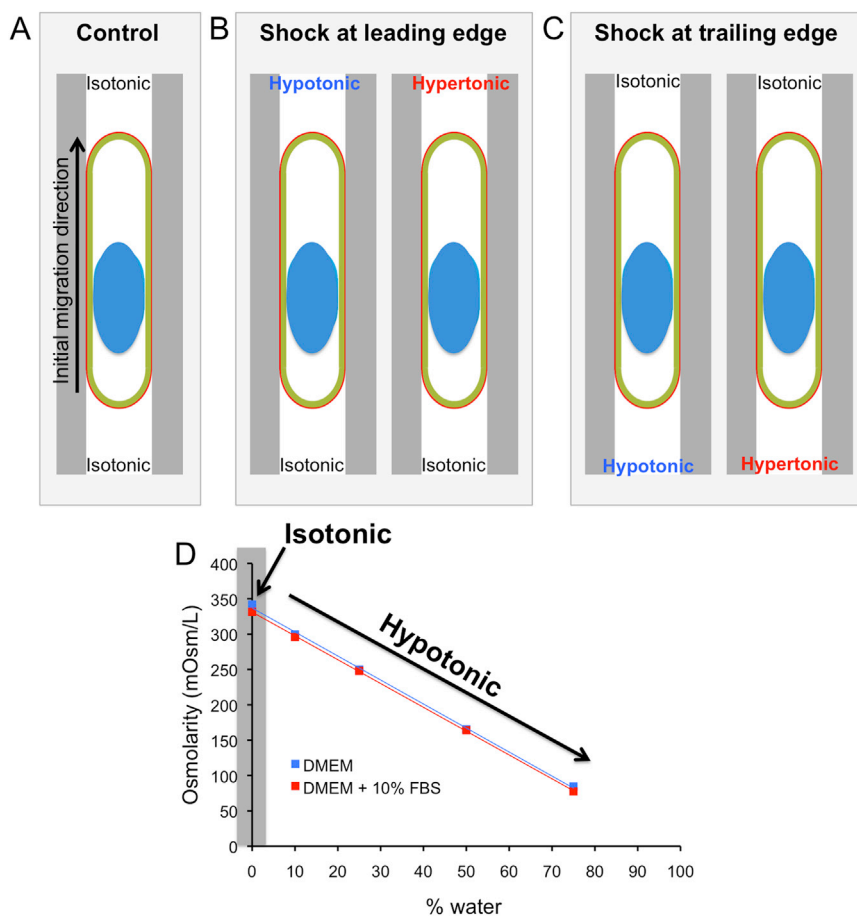
Figure S2. Methods for Applying Osmotic Shock in Confined Spaces, Related to Figure 2

Once cells had fully entered microfluidic channels, media was changed in all wells of the device to produce an osmotic shock at either the leading or trailing edge of the cell.

(A) Control case was produced by applying isotonic media at both the top and bottom of the chamber.

(B) Osmotic shock at the leading edge was produced by adding hypotonic or hypertonic media to the top inlets of the device and isotonic media to the bottom inlet of the device.

(C) Osmotic shock at the trailing edge was produced by adding hypotonic or hypertonic media to the bottom inlet of the device and isotonic media to the top inlets of the device.

(D) Hypotonic media was created by mixing DMEM (with or without FBS) with deionized, filtered water, and osmolarity was measured as a function of water percentage using an osmometer.
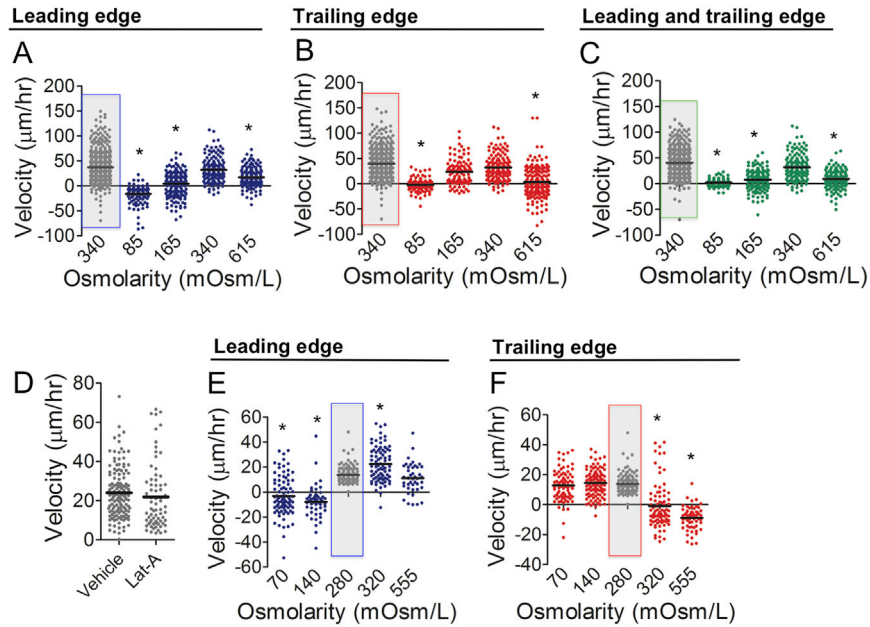
Figure S3. Velocity of Confined MDA-MB-231 and CH2879 Cells as a Function of Osmotic Shock, Related to Figure 3

(A–C) MDA-MB-231 cell velocity as a function of osmotic shock at the (A) leading edge, (B) trailing edge, or (C) both leading and trailing edges.

(D) Velocity of vehicle control- or Lat-A-treated CH2879 cells.

(E and F) Also shown is CH2879 cell velocity as a function of osmotic shock at the (E) leading edge or (F) trailing edge.

Gray boxes indicate migration velocity before shock, whereas data with white background represent an osmotic shock (or media change only, in the case of 340 mOsm/l control). *p < 0.05 in comparison with control (340 mOsm/l for MDA-MB-231 cells or 280 mOsm/l for CH2879 cells) by Student's t test. All migration experiments were performed in 3 μm-wide channels.
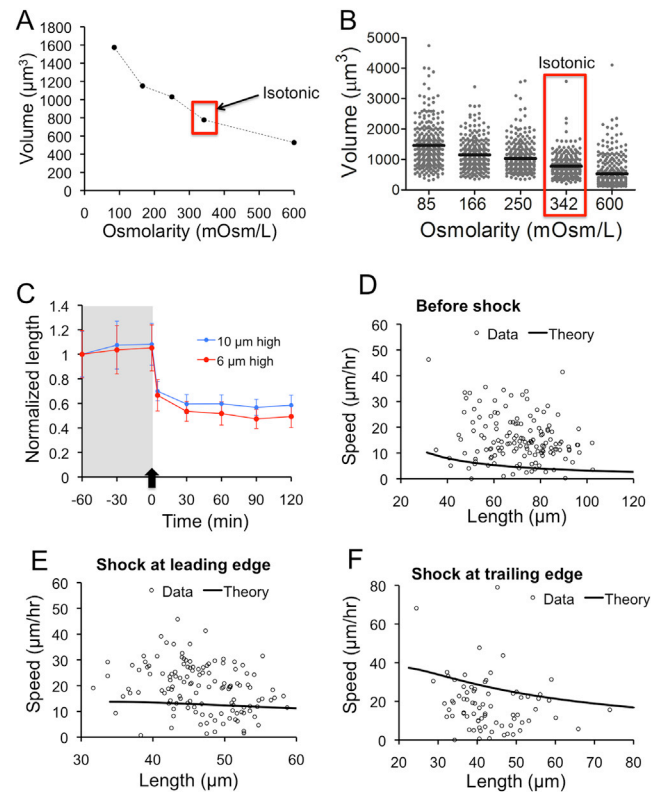
Figure S4. Cell Volume Changes upon Osmotic Shock, Related to Figure 4

(A) MDA-MB-231 volume (in suspension) as a function of osmolarity.

(B) Dot plot showing MDA-MB-231 volume (in suspension) as a function of osmolarity.

(C) Normalized S180 cell length in 10 μm or 6 μm high channels as a function of time after a hypotonic (165 mOsm/l) shock at the leading edge.

(D–F) Also shown is S180 cell speed as a function of cell length (D) before shock, (E) during the 30 min after hypotonic shock (165 mOsm/l) at the leading edge, or (F) during the 30 min after hypotonic shock (165 mOsm/l) at the trailing edge.

Bars indicate mean ± SD in (C). In (B), (D), (E), and (F), each data point represents one cell. Theoretical predictions are overlaid on data. All experiments were performed in 3 μm-wide channels.
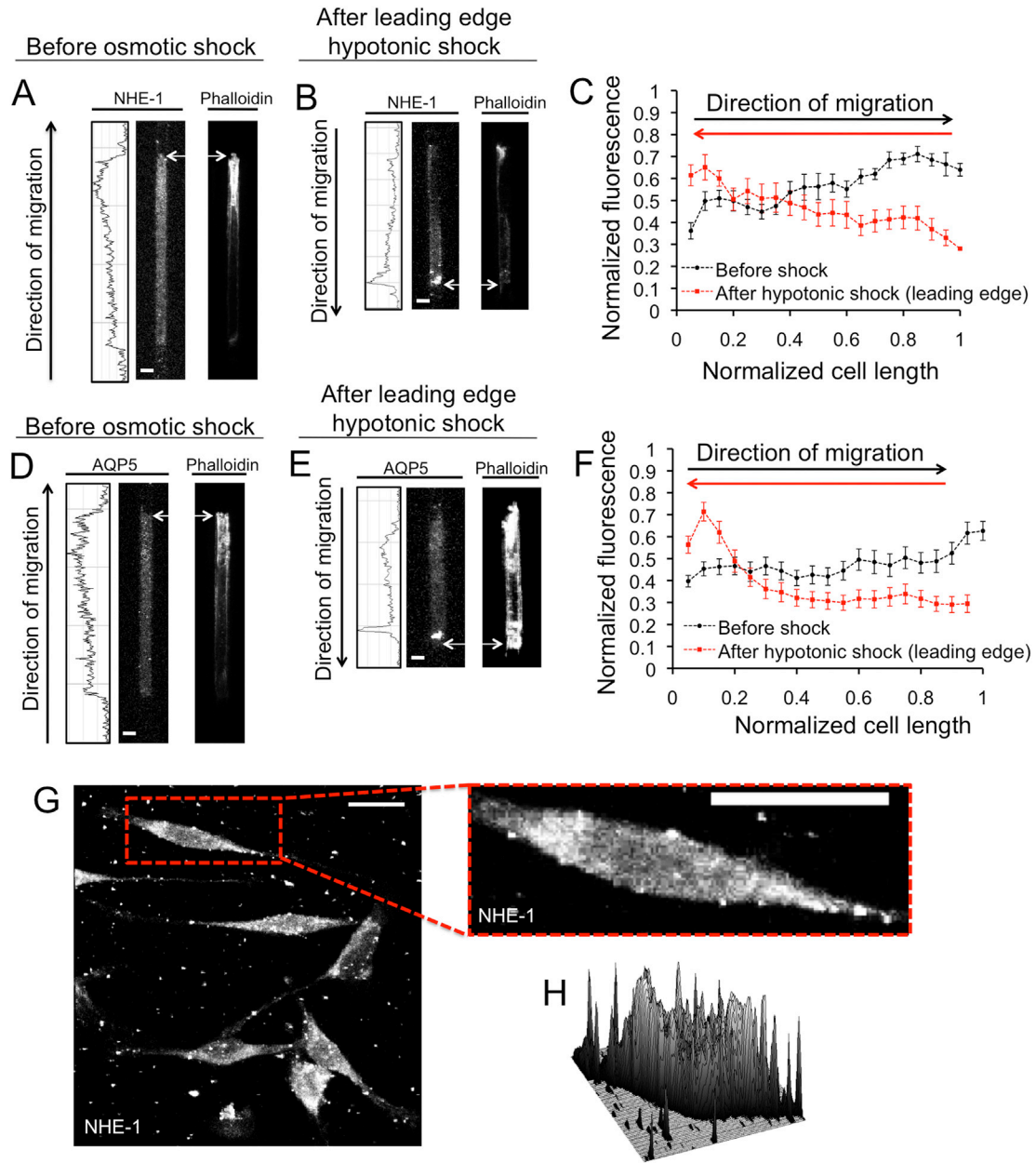
Figure S5. NHE-1 and AQP5 Polarize to the Leading Edges of Cells Migrating in Confinement, Related to Figure 5

(A and B) Confocal images and corresponding NHE-1 plot profiles of MDA-MB-231 cells stained for NHE-1 or for actin by phalloidin-Alexa 488, (A) in isotonic medium and (B) after a hypotonic shock (165 mOsm/l) at the leading edge. White scale bars represent 3 μm, whereas white arrows point to cell's leading edge.

(C) Normalized NHE-1 fluorescence intensity (to maximum value for each cell) as a function of the normalized cell length (to maximum cell length), for isotonic media and after a 165 mOsm/l hypotonic shock at the leading edge.

(D and E) Also shown are confocal images and corresponding AQP5 plot profiles of MDA-MB-231 cells stained for AQP5 or for actin by phalloidin-Alexa 488, (D) in isotonic medium or (E) 1 hr after a hypotonic (165 mOsm/l) shock at the leading edge. White scale bars represent 3 μm, whereas white arrows point to cell's leading edge.

(F) Normalized AQP5 fluorescence intensity (to maximum value for each cell) as a function of the normalized cell length (to maximum cell length), for isotonic conditions, or after a hypotonic (165 mOsm/l) shock at the leading edge of MDA-MB-231 cells.

Data points for (C) and (F) represent mean ± SEM of at least 25 cells, and all experiments were performed in 3 μm-wide channels.

(G and H) Confocal image and inset (G) and corresponding surface plot (H) of S180 cell shown in inset on a 2D planar surface. White scale bars represent 20 μm in (G).
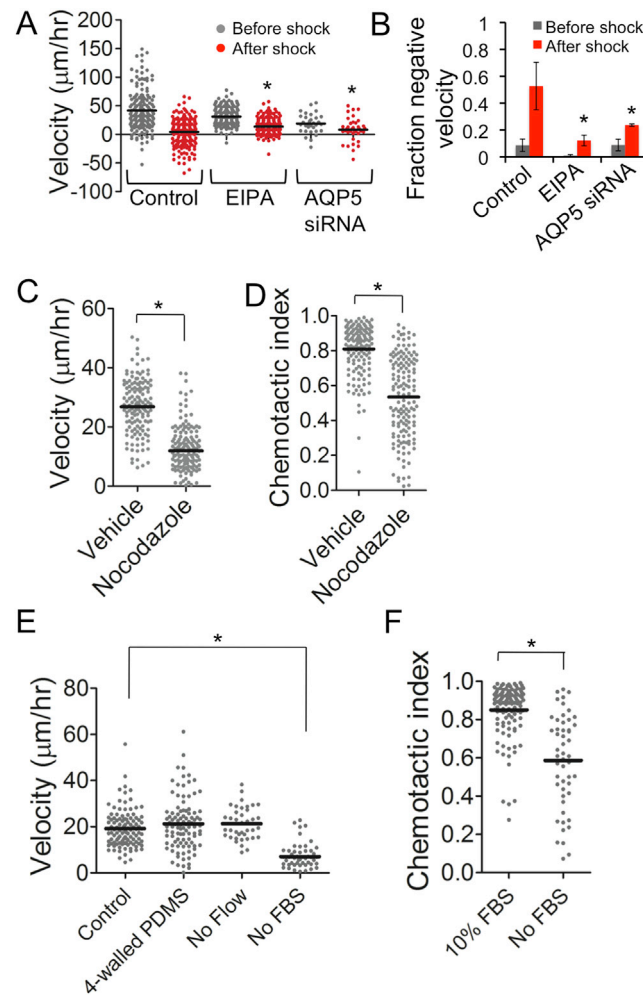
Figure S6. Inhibition of Na$^+$/H$^+$ Exchangers or Knockdown of AQP5 in MDA-MB-231 Cells, Related to Figure 6

(A) Velocity of MDA-MB-231 cells before (gray dots) and after (red dots) hypotonic shock (165 mOsm/l) at leading edge after 10 µM EIPA treatment or knockdown of AQP5.

(B) Fraction of MDA-MB-231 cells with negative velocity (i.e., that reverse direction) after 10 µM EIPA treatment or knockdown of AQP5. Bars represent mean ± SEM of three independent experiments.

In (A) and (B), * represents $p < 0.05$ in comparison with control data after shock.

(C and D) Velocity (C) and chemotactic index (D) of S180 cells before osmotic shock.

(E) Velocity of S180 cells in 4-walled PDMS channels, in the absence of flow, or with no FBS gradient.

(F) Chemotactic index of S180 cells in the absence of an FBS gradient.

*$p < 0.05$ in comparison with control by Student's t test. All experiments were performed in 3 µm-wide channels.